

# Revisiting the relationship between $6\ \mu\text{m}$ and 2–10 keV continuum luminosities of AGN

S. Mateos<sup>1\*</sup>, F. J. Carrera<sup>1</sup>, A. Alonso-Herrero<sup>1†</sup>, E. Rovilos<sup>2</sup>, A. Hernán-Caballero<sup>1</sup>, X. Barcons<sup>1</sup>, A. Blain<sup>3</sup>, A. Caccianiga<sup>4</sup>, R. Della Ceca<sup>4</sup>, P. Severgnini<sup>4</sup>

<sup>1</sup> *Instituto de Física de Cantabria (CSIC-Universidad de Cantabria), 39005, Santander, Spain*

<sup>2</sup> *Institute for Astronomy, Astrophysics, Space Applications & Remote Sensing, National Observatory of Athens, 15236 Palaia Penteli, Greece*

<sup>3</sup> *Physics and Astronomy, University of Leicester, University Road, Leicester LE1 7RH, UK*

<sup>4</sup> *INAF-Osservatorio Astronomico di Brera, via Brera 28, 20121 Milano, Italy*

Accepted 2015 February 11. Received 2015 February 10; in original form 2014 October 2

## ABSTRACT

We have determined the relation between the AGN luminosities at rest-frame  $6\ \mu\text{m}$  associated to the dusty torus emission and at 2–10 keV energies using a complete, X-ray flux limited sample of 232 AGN drawn from the Bright Ultra-hard XMM-Newton Survey. The objects have intrinsic X-ray luminosities between  $10^{42}$  and  $10^{46}\ \text{erg s}^{-1}$  and redshifts from 0.05 to 2.8. The rest-frame  $6\ \mu\text{m}$  luminosities were computed using data from the Wide-Field Infrared Survey Explorer and are based on a spectral energy distribution decomposition into AGN and galaxy emission. The best-fit relationship for the full sample is consistent with being linear,  $L_{6\ \mu\text{m}} \propto L_{2-10\ \text{keV}}^{0.99 \pm 0.03}$ , with intrinsic scatter,  $\Delta \log L_{6\ \mu\text{m}} \sim 0.35$  dex. The  $L_{6\ \mu\text{m}}/L_{2-10\ \text{keV}}$  luminosity ratio is largely independent on the line-of-sight X-ray absorption. Assuming a constant X-ray bolometric correction, the fraction of AGN bolometric luminosity reprocessed in the mid-IR decreases weakly, if at all, with the AGN luminosity, a finding at odds with simple receding torus models. Type 2 AGN have redder mid-IR continua at rest-frame wavelengths  $< 12\ \mu\text{m}$  and are overall  $\sim 1.3$ –2 times fainter at  $6\ \mu\text{m}$  than type 1 AGN at a given X-ray luminosity. Regardless of whether type 1 and type 2 AGN have the same or different nuclear dusty toroidal structures, our results imply that the AGN emission at rest-frame  $6\ \mu\text{m}$  is not isotropic due to self-absorption in the dusty torus, as predicted by AGN torus models. Thus, AGN surveys at rest-frame  $\sim 6\ \mu\text{m}$  are subject to modest dust obscuration biases.

**Key words:** galaxies: active-quasars: general-infrared: galaxies

## 1 INTRODUCTION

In the standard unified model of Active Galactic Nuclei (AGN), the observed differences between AGN sub-classes are solely explained as the result of an orientation effect with respect to an optically and geometrically thick distribution of molecular gas and dust on tens of parsecs scales, frequently assumed to have a toroidal geometry (Antonucci 1993; Urry & Padovani 1995). This material, hereafter referred to as the dusty torus, absorbs the AGN bolometric luminosity output produced at rest-frame UV/optical and X-ray wavelengths in the accretion disk/corona and re-emits it mainly in the mid-infrared (mid-IR) regime (rest-frame wavelengths  $\sim 5$ – $30\ \mu\text{m}$ ). Thus, it is clear that the mid-IR

spectral range offers a unique opportunity to study the obscured accretion phenomenon. Surveys conducted using data from Spitzer-IRAC have identified a population of highly obscured AGN whose number density is comparable to that observed for unobscured AGN. Many of these objects might be hidden at optical and X-ray wavelengths by Compton-thick material (line-of-sight rest-frame gas column densities  $N_{\text{H}} > 1.5 \times 10^{24}\ \text{cm}^{-2}$ ; Martínez-Sansigre et al. 2005).

Uncovering the mid-IR thermal continuum associated with the AGN dusty torus emission can be a difficult task, due to contamination from the AGN host galaxies. High (subarcsecond) spatial resolution observations can isolate the AGN emission from other contaminants on nearby objects with favourable geometries. Alternatively, mid-IR spectral decomposition can provide reliable estimates of the AGN dusty torus contribution to the infrared light (e.g. Ballo et al. 2014). Studies such as these have found

\*E-mail: mateos@ifca.unican.es

†Augusto G. Linares Senior Research Fellow

a tight correlation between the intrinsic luminosity, traced by hard (2-10 keV) X-rays, and reprocessed mid-infrared emission of AGN over more than three orders of magnitude in luminosity (Lutz et al. 2004; Ramos Almeida et al. 2007; Horst et al. 2008; Gandhi et al. 2009; Levenson et al. 2009; Asmus et al. 2011; Mason et al. 2012; Asmus et al. 2014). The relationship between hard X-ray and mid-IR luminosities seems to be identical for AGN optically classified as type 1 and type 2, even for Compton-thick AGN. If the hard X-ray emission is a good tracer of both the intrinsic power of AGN and the heating source of the dusty torus, then these studies provide strong observational support for the mid-IR light being a reliable proxy for the AGN intrinsic power, regardless of any obscuration. Unfortunately, the AGN samples involved in these studies are highly incomplete and biased towards infrared-bright objects. Recent studies of local AGN detected with the Swift Burst Alert Telescope and AKARI all-sky surveys have shown a tight correlation between the hard X-ray ( $>10$  keV energies) and monochromatic mid-IR (9 and  $18\mu\text{m}$ ) luminosities and that unabsorbed and absorbed AGN follow the same correlation (Ichikawa et al. 2012; Matsuta et al. 2012).

The sensitive all-sky infrared survey conducted with the Wide-field Infrared Survey Explorer (*WISE*; Wright et al. 2010) at 3.4, 4.6, 12 and  $22\mu\text{m}$  will dramatically increase our AGN census over a significant fraction of the age of the Universe improving greatly our understanding of the obscured accretion phenomenon in luminous systems. It has already been demonstrated that mid-IR colour-based selection techniques with *WISE*, targeting the characteristic red power-law thermal continuum emission from the AGN dusty torus ( $f_\nu \propto \nu^\alpha$  with  $\alpha \leq -0.5$ ; Alonso-Herrero et al. 2006), are highly reliable and effective at uncovering both unobscured and obscured luminous AGN (e.g. Assef et al. 2010; Mateos et al. 2012; Stern et al. 2012; Assef et al. 2013; Mateos et al. 2013; Yan et al. 2013). As demonstrated in Mateos et al. (2013), *WISE* can potentially uncover many Compton-thick AGN missed at other wavelengths, at least up to  $z \sim 1$ . Despite such progress, the physical properties of the AGN revealed with *WISE* remain poorly constrained.

In this paper we investigate how well we can isolate the AGN emission associated to the dusty torus in the mid-IR regime using the *WISE* broad band photometric data and, more importantly, whether the mid-IR continuum luminosities derived in this way are a reliable isotropic proxy for the intrinsic luminosity of AGN. To do so we have conducted a UV-to-mid-IR spectral energy distribution decomposition into AGN and galaxy components. Then we have studied the correspondence between the AGN luminosities at rest-frame  $6\mu\text{m}$ , corrected for the accretion disk and host galaxy emission, and at 2-10 keV energies over more than three orders of magnitude in AGN luminosity. We have used the final data release of the *WISE* survey (AllWISE; Cutri et al. 2013) and a large uniform complete sample of 232 X-ray selected AGN drawn from the Bright Ultra-hard XMM-Newton Survey. The objects have  $z$  in the range 0.05-2.8, and intrinsic (absorption-corrected) 2-10 keV X-ray luminosities between  $10^{42}$  and  $10^{46}\text{erg s}^{-1}$ . The X-ray luminosities, corrected for absorption, were computed from a detailed analysis of the *XMM-Newton* X-ray spectroscopic data available for all objects.

This paper is structured as follows. Section 2 describes

the AGN sample and the multiwavelength data used in this study. In Section 3 we describe the SED fitting approach used to isolate the AGN mid-IR emission, the adopted technique to compute rest-frame  $6\mu\text{m}$  luminosities and discuss the effects associated with contamination from the AGN host galaxies. In Section 4 we present the relationship between  $6\mu\text{m}$  and 2-10 keV continuum luminosities. The main results are discussed in Section 5 and summarized in Section 6. Throughout this paper errors are 68 per cent confidence for a single parameter, and we assume  $\Omega_M = 0.3$ ,  $\Omega_\Lambda = 0.7$  and  $H_0 = 70\text{ km s}^{-1}\text{ Mpc}^{-1}$ .

## 2 AGN SAMPLE DESCRIPTION

Our AGN sample was drawn from the wide-angle Bright Ultra-hard *XMM-Newton* Survey (BUXS; Mateos et al. 2012). BUXS is a large, complete, flux-limited sample of X-ray bright ( $f_{4.5-10\text{ keV}} > 6 \times 10^{-14}\text{ erg s}^{-1}\text{ cm}^{-2}$ ) AGN detected with the *XMM-Newton* observatory at 4.5-10 keV energies. The survey is based on 381 high Galactic latitude ( $|b| > 20^\circ$ ) *XMM-Newton* observations having good quality for serendipitous source detection that were used to derive extragalactic source count distributions at intermediate X-ray fluxes (Mateos et al. 2008). BUXS contains 255 AGN, after removal of Galactic stars and known BL Lacs ( $<3\%$ ), detected over a total sky area of  $44.43\text{ deg}^2$ .

### 2.1 UV/optical spectroscopic follow-up and AGN classification

All the sources in BUXS are in the area covered by the Sloan Digital Sky Survey (SDSS) imaging survey Data Release 7 in the *ugriz* bands (Abazajian et al. 2009). To identify the optical counterparts we used the likelihood-ratio estimator cross-matching algorithm of Pineau et al. (2011)<sup>1</sup> (see Mateos et al. 2012 for details). All sources but two have detections in SDSS. For the remaining two sources we identified their optical counterparts from our own imaging campaign.

Optical spectroscopic identifications and classifications are currently available for all but five objects. Such high identification completeness (98 per cent) guarantees that our study will not suffer from biases associated with low optical identification rates. The data has been collected from the literature (mainly from SDSS) and as part of our extensive optical follow-up identification programme (full details will be presented in a forthcoming paper).

Throughout this paper, objects with detected UV/optical emission line velocity widths  $\geq 1500\text{ km s}^{-1}$  and intermediate Seyfert types 1-1.5 are classified as type 1 AGN (143) while Seyfert types 1.8, 1.9 and 2 and those objects with a galaxy spectrum with no emission lines are classified as type 2 AGN (107). In this way we have a more uniform optical spectroscopic classification over the  $z$  range sampled by BUXS. For example, Seyfert 1.9s would be classified as type 2 AGN at  $z \gtrsim 0.2$ , when the  $\text{H}\alpha$  line

<sup>1</sup> The code is available from <http://saada.u-strasbg.fr/docs/fxp/plugin/>

**Table 1.** Summary of the main properties of the AGN used in this study.

| Sample | $N$ | $\Delta \log L_{2-10 \text{ keV}}$<br>erg s <sup>-1</sup> | $\langle \log L_{2-10 \text{ keV}} \rangle$<br>erg s <sup>-1</sup> | $\Delta z$  | $\langle z \rangle$ | $N_{\text{abs}}$   |
|--------|-----|---|--|-------------|---------------------|--------------------|
| (1)    | (2) | (3)   | (4)  | (5)         | (6)                 | (7)                |
| All    | 232 | 42.12-46.00   | 43.94(43.94)   | 0.056-2.860 | 0.558(0.396)        | 121(52.1 per cent) |
| Type 1 | 137 | 42.32-46.00   | 44.23(44.38)   | 0.061-2.860 | 0.713(0.646)        | 37(27.0 per cent)  |
| Type 2 | 95  | 42.12-45.19   | 43.52(43.41)   | 0.056-1.266 | 0.334(0.240)        | 85(89.5 per cent)  |

*Notes.* Column 1: sample; Column 2: number of sources; Column 3: 2-10 keV X-ray luminosity range (in logarithmic units). Column 4: Median (mean) X-ray luminosity (in logarithmic units); Column 5: redshift range; Column 6: median (mean) redshift; Column 7: number (fraction) of objects with detected X-ray absorption.

at 6563Å is redshifted from our optical spectra<sup>2</sup>. We have checked that the results of our study do not change if we instead classify Seyferts 1.8 and 1.9 as type 1 AGN.

## 2.2 Broad-band UV-to-mid-IR photometric data

As discussed below, one of the main goals of our study is to determine the rest-frame 6 μm mid-IR continuum emitted by the AGN dusty torus. To do so we have decomposed the rest-frame UV-to-mid-IR SEDs of our AGN into AGN and host galaxy components. To build the SEDs we have collected all the available photometric data from SDSS, the Two Micron All Sky Survey (2MASS), the UKIRT Infrared Deep Sky Survey (UKIDSS) and *WISE*.

We have used SDSS MODEL MAG magnitudes as they provide reliable estimates of the fluxes of extended objects while, for point sources, they are indistinguishable from the standard point spread function (PSF) magnitudes. We converted SDSS magnitudes and errors into flux densities following the SDSS recommendations<sup>3</sup>. A 2 per cent error was added in quadrature to the catalogued flux errors to account for the uncertainties in the zero-points.

We have used the cross-matching algorithm of Pineau et al. (2011) to identify the *WISE* mid-IR counterparts of our AGN (see Mateos et al. 2012 for details). All sources but six (five type 1 AGN and one type 2 AGN) have detections with SNR ≥ 2 at the *WISE* wavelengths of 3.4, 4.6 and 12 μm in AllWISE. The mean X-ray-mid-IR separation is ≲ 2 arcsec. Only 10 objects have a non-zero AllWISE photometric quality flag in at least one of the *WISE* bands indicating that the fluxes may be contaminated due to proximity to an image artefact (*cc\_flags*; Cutri et al. 2013). After a careful visual check of the *WISE* images and SEDs we found no issues in the *WISE* fluxes for any of the sources so we decided to keep them in our sample.

We computed flux densities in the *WISE* bands using either elliptical aperture magnitudes for the objects flagged as extended (six in total) or profile fitting photometry for the sources not spatially resolved. We used the magnitude zero points on the Vega system  $F_{\nu}(\text{iso}) = 309.124 \text{ Jy}$ ,  $171.641 \text{ Jy}$ ,  $30.988 \text{ Jy}$  and  $8.346 \text{ Jy}$  for 3.4, 4.6, 12 and 22 μm, respectively (Wright et al. 2010). They correspond to a spectrum  $f_{\nu} \propto \nu^{\alpha}$  with  $\alpha = -1$ . We added 1.5 per cent uncertainties

to the catalogued flux errors in all bands to account for the overall systematic uncertainty from the Vega spectrum in the flux zero-points. To account for discrepancies between the red and blue calibrators used for the conversion from magnitudes to Janskys we added an additional 10 per cent uncertainty to the 12 and 22 μm catalogued fluxes (Wright et al. 2010).

At the stage of the project when we searched for the near-IR photometric information available for all the AGN in BUXS we had already accurate source positions for the optical counterparts of all the objects in the sample. Therefore, to identify the near-IR counterparts of our AGN, we cross-correlated the coordinates of their optical counterparts with the Two Micron All Sky Survey (2MASS) catalogues of point and extended sources (Jarrett et al. 2000; Cutri et al. 2003) and the UKIRT Infrared Deep Sky Survey (UKIDSS) Data Release 10 catalogues (Lawrence et al. 2007) using a simple position matching with a search radius of 2 arcsec. In total 166 objects (~71 per cent) have detections in the near-IR. The mean optical-infrared separation is < 1 arcsec. We have checked that increasing the search radius does not produce any additional matches. From UKIDSS we used Petrosian magnitudes for extended sources and the default aperture magnitudes for point sources. As for SDSS, we added a 2 per cent error in quadrature to the catalogued flux errors to account for uncertainties in the zero-points. 2MASS and UKIDSS magnitudes were converted into fluxes using the zero points  $F_{\nu}(\text{iso}) = 1594 \text{ Jy}$ ,  $1024 \text{ Jy}$  and  $666.7 \text{ Jy}$  for the 2MASS *JHK<sub>s</sub>* (Cohen, Wheaton, & Megeath 2003) and  $F_{\nu}(\text{iso}) = 2232 \text{ Jy}$ ,  $2026 \text{ Jy}$ ,  $1530 \text{ Jy}$ ,  $1019 \text{ Jy}$  and  $631 \text{ Jy}$  for the UKIDSS *ZYJHK* (Hewett et al. 2006).

We note that if we use the *WISE* magnitude zero points in the Vega system corresponding to the spectral shapes assumed to convert magnitudes to flux densities in UKIDSS ( $\sim \nu^0$ ) and 2MASS ( $\sim \nu^{-2}$ ), the differences in the derived flux densities in the *WISE* bands would be lower than one per cent at 3.4, 4.6 and 22 μm and nine per cent at 12 μm, all below the systematic uncertainties in the catalogued fluxes.

## 2.3 X-ray spectral properties

Here we give a brief summary of the analysis conducted to determine the X-ray properties of our AGN. Full details on the X-ray spectral extraction procedure, analysis of the data and X-ray properties of the full sample of BUXS AGN will be presented in a forthcoming paper.

We have good quality *XMM-Newton* X-ray spectra in the observed energy range from 0.25 to 10 keV for all the AGN in this study. The median (mean) background sub-

<sup>2</sup> The optical spectra from our follow-up identification programme do not typically extend to wavelengths longer than ~8000Å.

<sup>3</sup> <http://www.sdss.org/dr7/algorithms/fluxcal.html>

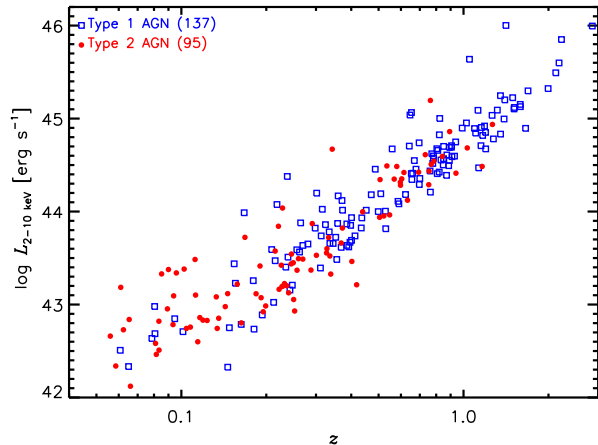


**Figure 1.** Hard X-ray luminosity versus  $z$  for the AGN in BUXS selected for this study.

tracted number of counts in the 0.25-10 keV EPIC spectra (MOS+pn) is 1443 (3127), where the counts range from 52 to 75,000. The X-ray spectroscopic analysis was conducted with the Xspec package (v12; Arnaud 1996). For each object we fitted the data with a combination of different models to determine the shape of the direct and scattered continuum components (modelled with power-laws) and rest-frame line-of-sight X-ray absorption (considering both full coverage and partial coverage of the continuum source). All models include the Galactic absorption for each source using column densities taken from Dickey & Lockman (1990). We have also accounted for the ‘soft excess’ i.e., any emission at energies  $\lesssim 1$  keV in excess of the extrapolation of the primary continuum, an almost ubiquitous feature in the X-ray spectra of AGN (e.g. Turner et al. 1997; Porquet et al. 2004; Guainazzi, Matt, & Perola 2005; Piconcelli et al. 2005; Mateos et al. 2010; Scott, Stewart, & Mateos 2012; Winter et al. 2012) using thermal and black-body models. To accept the detection of a model component we used the F-test with a significance threshold of 95 per cent.

If X-ray absorption was not detected we computed  $1\sigma$  upper limits using the best-fitting model parameters. Though BUXS includes many objects with X-ray absorption close to being Compton-thick, when taking into account the uncertainties in the best-fit rest-frame column densities, all X-ray absorption values are consistent with being in the Compton-thin regime ( $N_{\text{H}} < 1.5 \times 10^{24} \text{ cm}^{-2}$ ). Thus, based on the existing X-ray data we do not have any securely confirmed Compton-thick AGN. The X-ray luminosities used in this paper have been determined from the best-fit models in the rest-frame 2-10 keV energy band and are corrected for X-ray absorption. Examples of our X-ray spectral modelling are shown in Fig. 2.

## 2.4 AGN sample selection

For the study presented here we have selected the 232 AGN in BUXS with absorption-corrected X-ray luminosities  $\geq 10^{42} \text{ erg s}^{-1}$  and *WISE* detections in the three shortest wavelength bands (3.4, 4.6 and  $12 \mu\text{m}$ ) with  $\text{SNR} \geq 2$ . Out of these, 137 objects are type 1 AGN (122 Seyfert 1s, 15 Seyfert

1.5s) and 95 type 2 AGN (3 Seyfert 1.8s, 14 Seyfert 1.9s and 78 Seyfert 2s). The X-ray luminosity limit has been imposed to reduce to a minimum the effects of host galaxy contamination in the mid-IR regime by increasing the contrast of the AGN contribution.

The selected AGN have 2-10 keV X-ray luminosities between  $10^{42}$  and  $10^{46} \text{ erg s}^{-1}$  and  $z$  in the range 0.05-2.8. Table A1 lists the optical spectroscopic classification and intrinsic X-ray luminosity for all the AGN used in our study while Table 1 summarizes their main properties. The distribution of their  $z$  and 2-10 keV luminosities is shown in Fig. 1.

## 3 AGN MID-IR CONTINUUM LUMINOSITIES

Our study aims to investigate how well we can isolate the mid-IR emission associated with the AGN dusty torus using *WISE* broad band photometric data, and whether the mid-IR AGN luminosities determined in this way are a reliable isotropic proxy of the AGN intrinsic power. To do so we have studied the correspondence between the rest-frame  $6 \mu\text{m}$  and 2-10 keV X-ray continuum luminosities for our complete, flux-limited sample of X-ray selected AGN.

We have used rest-frame  $6 \mu\text{m}$  monochromatic luminosities as a tracer of the AGN dusty torus emission. As such emission can be well approximated by a power-law (see, e.g. Neugebauer et al. 1979; Elvis et al. 1994; Richards et al. 2006; Assef et al. 2010), to compute the  $6 \mu\text{m}$  luminosities we have used a simple linear interpolation/extrapolation in log-log space between the *WISE* catalogued fluxes at 4.6 and  $12 \mu\text{m}$ . Sec. 3.1 describes in detail how we corrected these luminosities for both host galaxy contamination and for the emission from the AGN accretion disk.

We have not used the *WISE*  $3.4 \mu\text{m}$  fluxes because, as shown in Sec. 3.1, they are severely contaminated by starlight. Moreover, we have not used the *WISE*  $22 \mu\text{m}$  fluxes because, as this survey is much shallower than the ones conducted at shorter wavelengths, many of our objects are not detected. Indeed, out of the 232 AGN selected for this study just 168 (72.4 per cent) are detected with  $\text{SNR} \geq 2$  at  $22 \mu\text{m}$ .

### 3.1 SED decomposition into the AGN and their hosts

Even at the high AGN luminosities involved in our study, the 4.6 and  $12 \mu\text{m}$  fluxes (rest-frame  $\sim 1.5\text{-}4 \mu\text{m}$  at  $z \sim 2$ ) might be contaminated by the emission from the AGN host galaxies. To isolate the AGN component and derive the  $6 \mu\text{m}$  luminosity associated with the dusty torus, we have decomposed the rest-frame UV-to-mid-IR SEDs of our objects into AGN and galaxy emission. We used the best-fit results to correct the  $6 \mu\text{m}$  luminosities for contamination from the AGN host galaxies and accretion disk emission. We stress that the main goal of the SED fitting analysis is to properly model all the continuum components in the observed SEDs to ensure a reliable determination of the dusty torus emission. We have used the fitting code SED Analysis us-



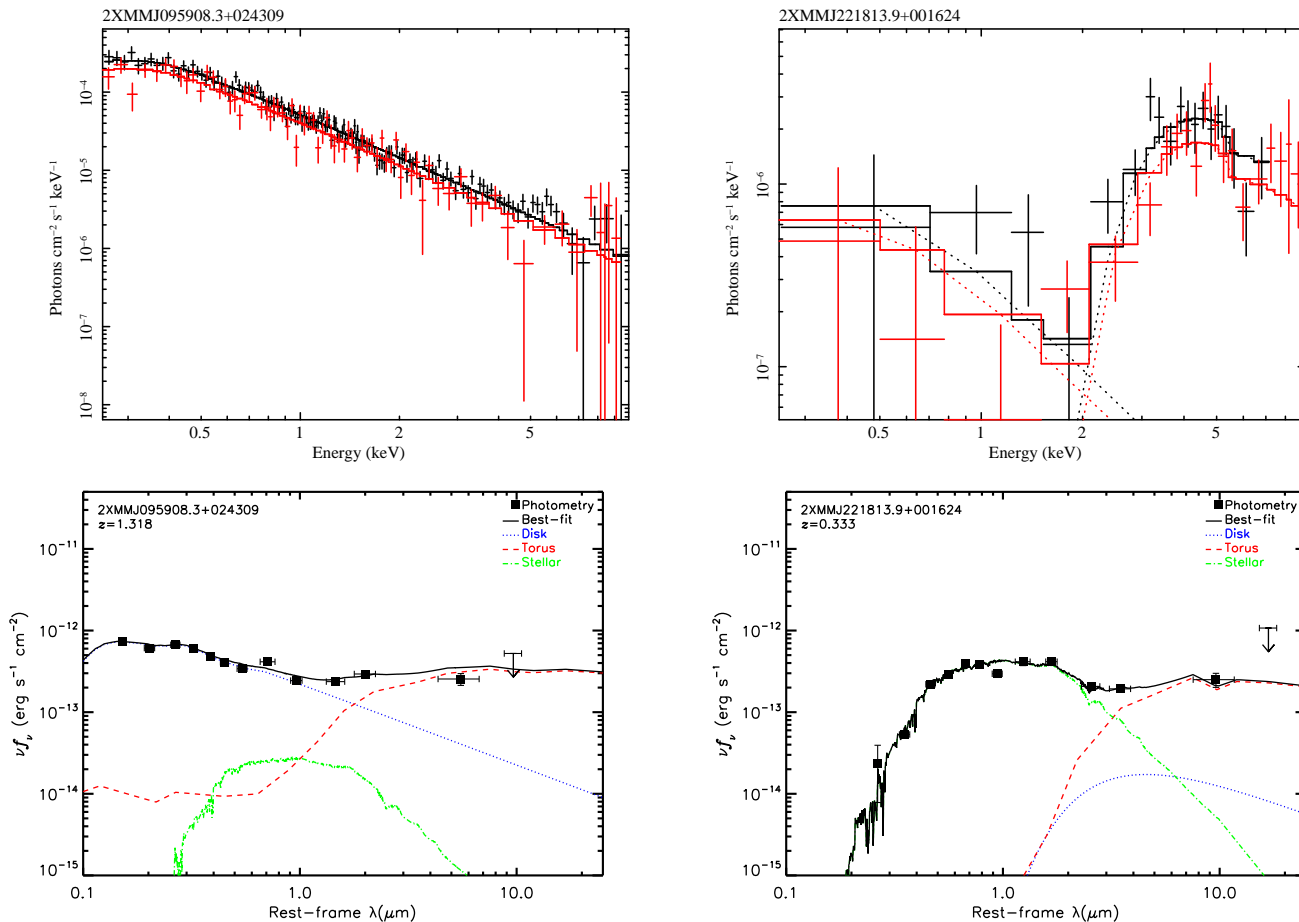


**Figure 2.** Examples of the modelling of the *XMM-Newton* EPIC X-ray spectroscopic data and SED decomposition for AGN classified as type 1 (left plots) and type 2 (right plots), respectively. Top: The X-ray spectra for 2XMMJ095908.3+024309 are best modelled with a simple unabsorbed power-law model (broad-band photon index  $\Gamma=1.88\pm 0.02$ ; solid lines). For 2XMMJ221813.9+001624 the best-fit model consists on an absorbed power-law ( $\Gamma=1.77^{+0.39}_{-0.37}$  and  $N_{\text{H}}=40.4^{+8.0}_{-7.1}$ , where the column density is in units of  $10^{22} \text{ cm}^{-2}$ ) plus a low-energy scattered power-law with same spectral index as that of the direct absorbed component (dotted lines). Bottom: The figures clearly illustrate that, at the shortest wavelength bands of *WISE*, the emission from the AGN host galaxies can dominate over that of the dusty torus especially in type 2 AGN where the extinction of the AGN emission is systematically higher.

ing Bayesian Statistics (SEABAS)<sup>4</sup> described in detail in Rovilos et al. (2014). The program uses the maximum likelihood method and a Monte Carlo Markov chain (MCMC) sampling technique to determine both the optimum combination of SED templates and the associated uncertainties.

### 3.1.1 SED components

We fitted the SEDs with three model components to reproduce the emission from the AGN accretion disk, the dusty torus and the stellar emission of the hosts.

To describe the UV/optical emission from the accretion disk we have used the average type 1 quasar SED of Richards et al. (2006) at  $\lambda < 0.7 \mu\text{m}$  and a power-law  $\lambda f_{\lambda} \propto \lambda^{-1}$  at longer wavelengths. To redden the accretion disk we have used the Gordon & Clayton (1998) Small Magellanic Cloud (SMC) extinction law at  $\lambda < 3300 \text{ \AA}$ , as it best

represents the nuclear reddening of quasars (Hopkins et al. 2004), while at  $\lambda > 3300 \text{ \AA}$  we used the Galactic extinction law from Cardelli, Clayton, & Mathis (1989). In both cases we assume  $R_V=3.1$ .

We have characterized the mid-IR emission from the AGN dusty torus with the template library of Silva, Maiolino, & Granato (2004). The library includes four templates divided according to the amount of X-ray absorption. These templates were generated by combining the nuclear mid-IR observations of a large sample of Seyfert galaxies and interpolation using the smooth-density dust emission model of Granato & Danese (1994). Of these we have used the Seyfert 1 template and the two Seyfert 2 templates corresponding to X-ray column densities in the Compton-thin regime:  $10^{22} < N_{\text{H}} < 10^{23} \text{ cm}^{-2}$  and  $10^{23} < N_{\text{H}} < 10^{24} \text{ cm}^{-2}$ . We have not used either the optical classification or best-fit X-ray column densities to choose amongst torus templates i.e., we have considered all three torus templates to fit the SEDs of our type 1 and type 2 AGN.

<sup>4</sup> <http://astro.dur.ac.uk/~erovilos/SEABAS/>

Finally, we have reproduced the emission from the stellar population of the AGN hosts at rest-frame optical-near-IR wavelengths with the stellar population synthesis models of Bruzual & Charlot (2003). We used a library of 75 stellar templates with solar metallicity and a Chabrier initial mass function (Chabrier 2003). We have used ten exponentially decaying star formation histories with characteristic times  $\tau=0.1$  to 30 Gyr and a model with constant star formation, and a set of ages in the range 0.1 to 13 Gyr (see Lusso et al. 2013 for a similar approach). We have checked that none of our fits require such long ( $> 10$  Gyr) and probably unphysical ages. We reddened the templates using the Calzetti et al. (2000) dust extinction law and a range of  $E(B-V)_{\text{gal}}$  from 0 to 2.

To avoid degeneracies between the AGN and galaxy templates, we have ignored any possible contamination from dust heated by star formation in the AGN hosts. As demonstrated in Sec. 3.3, at the high AGN luminosities involved in our study and rest-frame wavelengths sampled with the *WISE* 4.6 and 12  $\mu\text{m}$  surveys, contamination due to star formation has a negligible effect on our results. Nevertheless, as the star formation emission rapidly increases at rest-frame wavelengths  $\gtrsim 8 \mu\text{m}$ , contamination of the *WISE* 22  $\mu\text{m}$  fluxes might not be negligible at the lowest redshifts (and AGN luminosities). To minimize the impact of such effect we have treated all 22  $\mu\text{m}$  detections (168 in total) as upper limits.

In the following subsections, we discuss in more detail the SED fitting procedure and summarize the main results. In the AGN with signatures of the Broad Line Region in their rest-frame UV/optical spectrum (i.e. Seyfert types 1 to 1.9) the contamination from the accretion disk at UV/optical and near-IR wavelengths is not negligible. Therefore we have carried out the SED fits following a different approach for AGN with detected UV/optical broad emission lines (i.e. where we have a relatively unobscured view of the BLR and accretion disk; Sec. 3.1.2) and for AGN without detected UV/optical broad emission lines (i.e. where the accretion disk emission is highly obscured; Sec. 3.1.3). Nevertheless, we remind the reader that, to have a more uniform optical spectroscopic classification over the  $z$  range sampled by BUXS, throughout the paper we have classified Seyfert 1.8-1.9 (17 in total) as type 2 AGN (see Sec. 2.1).

### 3.1.2 SED fitting of AGN with detected UV/optical broad emission lines

For the type 1 AGN (137) and intermediate Seyfert types 1.8-1.9 (17) we have used a range of reddening values for the accretion disk,  $E(B-V)_{\text{disk}}$ , between 0 and 0.65 with a step  $\Delta E(B-V)_{\text{disk}}=0.01$ . As indicated in Caccianiga et al. (2008), the separation between optical type 1 and type 2 AGN corresponds to  $A_V \sim 2$  mag, or  $E(B-V) \sim 0.65$  assuming a Galactic standard conversion. To take into account any intrinsic dispersion in the SEDs of our AGN, the normalizations of the disk and torus components were left free to vary. The SED fitting was conducted both with and without the stellar component. We accepted the detection of the stellar component if the  $\chi^2$  difference between models,  $\Delta\chi^2$ , was higher than

6.17 ( $2\sigma$  confidence for two parameters)<sup>5</sup>. Otherwise we did not apply any correction for host galaxy contamination to the observed *WISE* fluxes.

We have found a median (mean) nuclear extinction  $E(B-V)_{\text{disk}}=0.05$  (0.11), with 68 per cent of the sources having  $E(B-V)_{\text{disk}}$  below 0.1. Considering only those sources showing evidence for both X-ray absorption (see Sec. 2.3) and UV/optical reddening (49 in total), we found that the great majority (88 per cent) have dust-to-gas ratios  $E(B-V)/N_{\text{H}}$  lower than Galactic by a factor varying from 1.5 to more than 100 in a few cases, in good agreement with Maiolino et al. (2001). In 42 objects (38 with  $L_{2-10 \text{ keV}} > 10^{44} \text{ erg s}^{-1}$ ) adding the stellar component did not improve the quality of the fit above the selected threshold. The median (mean) contribution of the accretion disk at rest-frame 6  $\mu\text{m}$ , relative to the best-fit torus model, is  $11.8_{-6.1}^{+7.6}$  ( $12.9 \pm 7.8$ ) per cent and has no significant luminosity dependence based on the Spearman's rank test (correlation coefficient  $\rho=-0.12$  and probability to reject the null hypothesis 86.7 per cent). The median uncertainty associated with the correction for the accretion disk emission determined from the SED fits is 13 per cent. Such uncertainties were added in quadrature to our 6  $\mu\text{m}$  luminosity estimates.

### 3.1.3 SED fitting of AGN without detected UV/optical broad emission lines

In the 78 AGN without detected broad emission lines in their rest-frame UV/optical spectra the accretion disk emission is highly obscured and the observed fluxes at rest-frame UV-to-near-IR wavelengths are dominated by the AGN host galaxies. Nevertheless, for AGN with nuclear reddening levels  $A_V \sim 2-5$  mag, the accretion disk emission at near-IR wavelengths ( $\sim 1-2 \mu\text{m}$ ) could still be relevant. As for these objects we do not have a direct view of the accretion disk, we cannot constrain both the extinction and normalization of such a component. The approach we followed was to fix the normalization of the accretion disk relative to the torus component to the median value obtained for the AGN with detected UV/optical broad lines. We then created a library of reddened accretion disk templates using a range of  $E(B-V)_{\text{disk}}$  values between 0.65 and 10 with a step  $\Delta E(B-V)_{\text{disk}}=0.15$ . These templates were added to each of the three torus templates used for the SED fitting. We repeated the fitting process, fixing the accretion disk normalization relative to the torus component to the median- $1\sigma$  and median+ $1\sigma$  values, and used the best-fit results to determine the uncertainties in the correction of the 6  $\mu\text{m}$  luminosities for the accretion disk emission.

The best-fit  $E(B-V)_{\text{disk}}$  values have a nearly uniform distribution between the chosen limits with a median (mean) value of  $E(B-V)_{\text{disk}}=6.22$  (5.95). We stress, however, that the measured nuclear extinctions should be regarded as less accurate than for objects where we have a direct view of the accretion disk. The median (mean) contribution of the reddened accretion disk at rest-frame 6  $\mu\text{m}$ , relative to the

<sup>5</sup> The relationship between  $\Delta\chi^2$  and the log-likelihood difference is  $\Delta\chi^2 = -2\Delta(\ln L)$  (see Appendix A in Rovilos et al. 2014 for details).

**Table 2.** Contribution from the reddened accretion disk and the AGN hosts to the mid-IR at rest-frame  $6\mu\text{m}$ .

| Sample | $N$ | $\Delta \log L_{2-10\text{ keV}}$<br>erg s $^{-1}$ | $f_{6\mu\text{m}}^{\text{st}}$<br>per cent | $f_{6\mu\text{m}}^{\text{disk}}$<br>per cent | $f_{6\mu\text{m}}^{\text{disk+st}}$<br>per cent | $f_{6\mu\text{m}}^{\text{sb}}$<br>per cent         |
|--------|-----|--|--|--|---|--|
| (1)    | (2) | (3)  | (4)  | (5)  | (6)   | (7)  |
| All    | 36  | 42-43  | $20.76^{+22.81}_{-15.88}$                  | $3.66^{+11.57}_{-2.47}$                      | $28.13^{+17.94}_{-11.23}$                       | $7.93^{+8.92}_{-4.79}$                             |
| Type 1 | 12  | 42-43  | $10.95^{+16.97}_{-8.13}$                   | $15.23^{+14.96}_{-5.72}$                     | $27.15^{+18.46}_{-10.25}$                       | $7.52^{+9.32}_{-5.38}$                             |
| Type 2 | 24  | 42-43  | $26.02^{+19.95}_{-14.94}$                  | $2.94^{+2.32}_{-2.16}$                       | $29.25^{+17.13}_{-12.37}$                       | $9.53^{+7.72}_{-5.60}$                             |
| All    | 86  | 43-44  | $7.81^{+8.93}_{-5.10}$                     | $7.39^{+7.18}_{-4.07}$                       | $17.96^{+8.73}_{-6.36}$                         | $2.54^{+3.20}_{-1.89}$                             |
| Type 1 | 39  | 43-44  | $5.09^{+6.78}_{-3.99}$                     | $10.79^{+6.09}_{-5.23}$                      | $18.32^{+8.55}_{-8.54}$                         | $1.65^{+2.56}_{-1.18}$                             |
| Type 2 | 47  | 43-44  | $11.57^{+5.91}_{-6.12}$                    | $5.94^{+3.83}_{-3.18}$                       | $17.41^{+8.26}_{-5.63}$                         | $3.19^{+3.22}_{-1.91}$                             |
| All    | 88  | 44-45  | $2.12^{+2.30}_{-2.12}$                     | $10.82^{+5.25}_{-5.87}$                      | $13.84^{+7.08}_{-4.34}$                         | $0.37^{+0.93}_{-0.25}$ ( $3.72^{+9.29}_{-2.46}$ )  |
| Type 1 | 65  | 44-45  | $1.40^{+2.67}_{-1.40}$                     | $11.40^{+6.74}_{-5.22}$                      | $14.18^{+6.88}_{-4.68}$                         | $0.32^{+0.62}_{-0.21}$ ( $3.25^{+6.17}_{-2.14}$ )  |
| Type 2 | 23  | 44-45  | $4.40^{+5.18}_{-2.88}$                     | $8.73^{+3.60}_{-4.11}$                       | $13.17^{+4.10}_{-2.91}$                         | $0.63^{+1.33}_{-0.44}$ ( $6.27^{+13.30}_{-4.45}$ ) |
| Type 1 | 21  | 45-46  | $0.23^{+0.83}_{-0.23}$                     | $11.33^{+4.23}_{-5.54}$                      | $12.45^{+6.94}_{-6.20}$                         | $0.01^{+0.05}_{-0.01}$ ( $0.11^{+0.65}_{-0.06}$ )  |

*Notes.* Column 1: sample; Column 2: number of sources; Column 3: 2-10 keV X-ray luminosity range (in logarithmic units). Columns 4 and 5: median contribution from the AGN hosts stellar emission and the reddened accretion disk at rest-frame  $6\mu\text{m}$ , respectively.

Column 6: median of the sum of the contributions from the AGN hosts and the reddened accretion disk at rest-frame  $6\mu\text{m}$ . Column 7: (very conservative) median upper limits for the level of contamination from star formation at rest-frame  $6\mu\text{m}$  assuming that the AGN hosts are LIRGs or ULIRGs (values in brackets; see Sec. 3.3 for details). The error bars represent the 16 and 84 percentiles. In the cases where the lower limit of the error bar reached zero, the upper limit corresponds to the 68 percentile (i.e., smallest interval that encloses the 68 per cent probability). Please note that to compute the numbers we have not included the only type 2 AGN in the sample with

$$L_{2-10\text{ keV}} > 10^{45}\text{ erg s}^{-1}.$$

best-fit torus model, is  $6.5^{+3.9}_{-2.6}$  ( $6.9\pm 3.3$ ) per cent. The median uncertainty associated with the correction for the accretion disk emission from the SED fits is 46 per cent. Although as pointed out previously, the extinction values are less accurate, we found that 67 per cent of the sources have dust-to-gas ratios lower than Galactic by a factor that varies from  $\sim 1.5$  to 90, again in very good agreement with Maiolino et al. (2001).

Examples of the SED fitting procedure for type 1 and type 2 AGN are shown in Fig. 2. The contamination from the AGN host galaxies at rest-frame near-IR and mid-IR wavelengths is discussed in Sec. 3.2 and Sec. 3.3 and summarized in Fig. 3 and Fig. 4. In Table 2 we report the median contribution from the AGN hosts and the reddened accretion disk at rest-frame  $6\mu\text{m}$  for type 1 and type 2 AGN at different X-ray luminosities.

### 3.2 Stellar contamination in the rest-frame near-IR and mid-IR

We have corrected our rest-frame  $6\mu\text{m}$  luminosities for the Rayleigh-Jeans tail of the emission of the different underlying stellar populations of the AGN host galaxies as follows. First, we have computed the observed fluxes in the 4.6 and  $12\mu\text{m}$  passbands associated with starlight emission using the best-fit stellar templates. To accurately reproduce the measurement process with the wide bandpasses of the *WISE* filters we have convolved the best-fit stellar SEDs with the *WISE* relative spectral response (RSR) filter curves. Then we have determined the luminosity at  $6\mu\text{m}$  associated with starlight emission through linear interpolation/extrapolation in log-log space. The median uncertainty associated with the correction for stellar emission deter-

mined from the SED fits is 19 per cent. These were added in quadrature to our  $6\mu\text{m}$  luminosity uncertainties.

Fig. 3 shows the relative contribution from starlight to the fluxes measured with *WISE* at 3.4, 4.6 and  $12\mu\text{m}$  as a function of AGN luminosity. In the cases where the emission from the AGN hosts was not detected with sufficient significance ( $\Delta\chi^2 < 6.17$ ) we assigned a zero value to the fractions. For AGN optically classified as type 2, the starlight contamination to the *WISE* fluxes at 3.4 and  $4.6\mu\text{m}$  is important across the full luminosity range sampled by our study. This is expected as dust extinction of the AGN emission is more important in type 2 objects. In addition, in flux-limited surveys, such as BUXS, the most luminous objects are detected at higher  $z$  and the *WISE* passbands are sampling shorter rest-frame wavelengths where the starlight emission peaks. As dust extinction of the AGN emission is less severe in type 1 objects, the starlight contamination to their mid-IR fluxes is significantly smaller than that for type 2 AGN but still non-negligible, especially at  $3.4\mu\text{m}$  (Kotilainen et al. 1992; Alonso-Herrero, Ward, & Kotilainen 1996; Alonso-Herrero et al. 2003). Only the *WISE* fluxes at  $12\mu\text{m}$  are dominated by the AGN at all luminosities, at least up to  $z\sim 2$ . An alternative way to visualize the dependence of the level of stellar contamination to the *WISE* fluxes on the AGN luminosity and optical class is representing the distribution of *WISE* colours for our sources. If we adopt the mid-IR colour definition of Mateos et al. (2012) (i.e.  $\log(f_{4.6\mu\text{m}}/f_{3.4\mu\text{m}})$  vs.  $\log(f_{12\mu\text{m}}/f_{4.6\mu\text{m}})$  flux density ratios), the most contaminated objects should be located in the bottom-right part of the colour-colour diagram. Indeed as we see in Fig. 6 in Mateos et al. (2012) the less luminous objects, in particular those classified as type 2 AGN, have overall the bluest  $\log(f_{4.6\mu\text{m}}/f_{3.4\mu\text{m}})$  mid-IR colours.

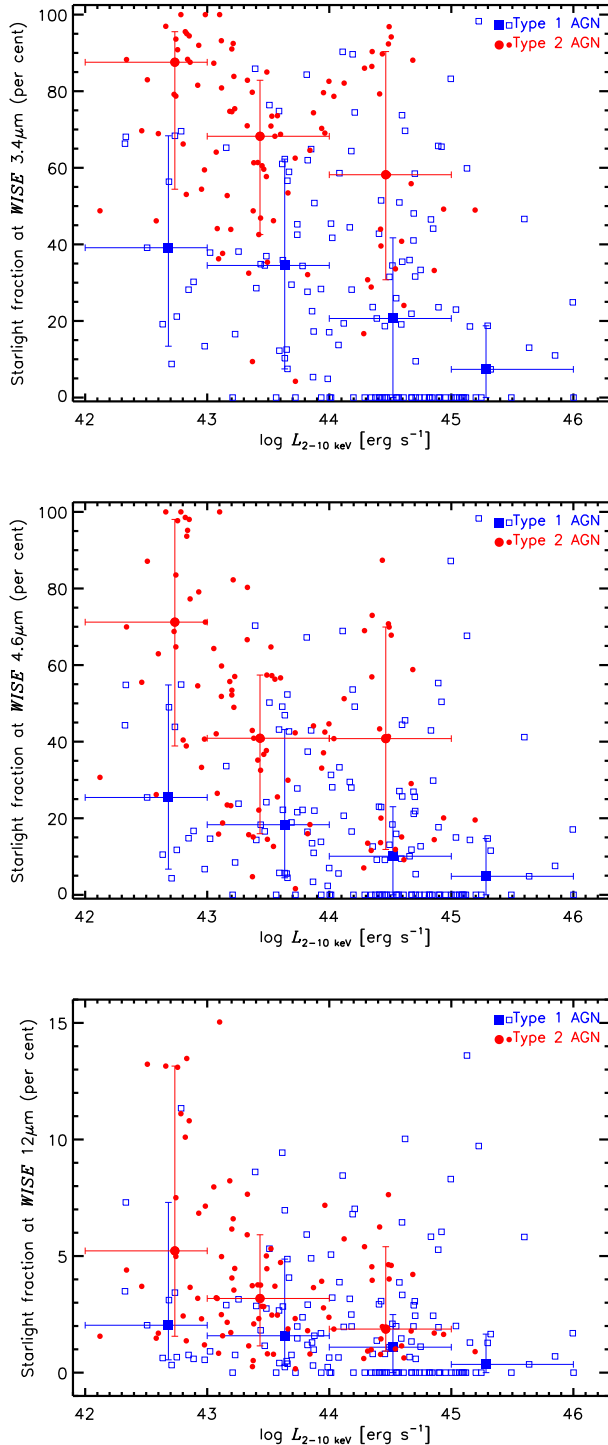


**Figure 3.** Contribution from the AGN host galaxies to the mid-infrared fluxes measured with *WISE* at 3.4, 4.6 and 12  $\mu\text{m}$  (observed frame). Large filled symbols and vertical error bars indicate the median and 16 and 84 percentiles (68 per cent enclosed, equivalent to  $1\sigma$ ) of the distribution of values in different luminosity intervals indicated with the horizontal error bars. In the cases where the lower limit of the error bar reached zero, the upper limit corresponds to the 68 percentile (i.e., smallest interval that encloses the 68 per cent probability).

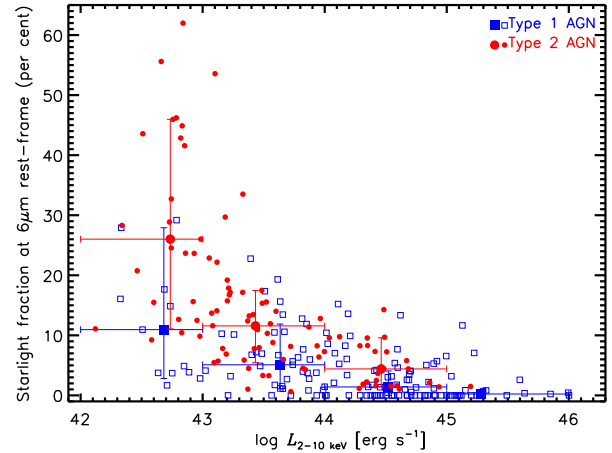


**Figure 4.** Host galaxy contribution to the rest-frame 6  $\mu\text{m}$  luminosities as a function of the AGN luminosity. Large filled symbols and vertical error bars indicate the median and the 16 and 84 percentiles (68 per cent enclosed, equivalent to  $1\sigma$ ) of the distribution of values in different luminosity intervals indicated with the horizontal error bars. In the cases where the lower limit of the error bar reached zero, the upper limit corresponds to the 68 percentile (i.e., smallest interval that encloses the 68 per cent probability).

Fig. 4 illustrates the correction for starlight emission to our rest-frame 6  $\mu\text{m}$  luminosities computed as indicated above. The corresponding values are reported in Table 2.

### 3.3 Contamination from star formation in the rest-frame mid-IR

As indicated in Sec. 3.1.1, we have not corrected our 6  $\mu\text{m}$  luminosities for the emission from dust in star forming regions in the AGN hosts. For example, Polycyclic Aromatic Hydrocarbon (PAH) features can probe star formation in the AGN hosts over time scales of tens of millions of years (e.g. Peeters, Spoon, & Tielens 2004). Nevertheless, it is expected that any PAH redshifted into the *WISE* observed bands superimposed on the strong AGN continuum would be smoothed out due to the wide bandpasses of the filters, especially for the extremely wide 12  $\mu\text{m}$  filter. To demonstrate that this is the case, we have determined upper limits on the level of contamination from star formation to our 6  $\mu\text{m}$  luminosities. To do so we have used the main sequence and starburst galaxy templates from Elbaz et al. (2011). For each object in our sample we have determined the upper limit in the normalization of the starforming templates assuming that the hosts of our AGN are Luminous Infrared Galaxies (LIRGs) with  $L_{8-1000 \mu\text{m}} \leq 6 \times 10^{11} L_{\odot}$  and star formation rates (SFRs) of  $\sim 100 M_{\odot} \text{yr}^{-1}$  based on the Kennicutt (1998) relation. The less than equal sign indicates the additional constraint that none of the fluxes determined from each template in the *WISE* bands (taking into account the filter RSRs) should be above the observed values. Then we computed the 6  $\mu\text{m}$  luminosities from linear interpolation/extrapolation of the 4.6 and 12  $\mu\text{m}$  fluxes in log-log space as we did for the original data. Following this approach we found that the contribution from star formation at 6  $\mu\text{m}$  is well below 15 per cent for 83.3 per cent of the



**Table 3.** Summary of the results of the linear regression analysis.

| Sample<br>(1) | Method<br>(2) | $N$<br>(3) | $\rho$ ( $p$ -value)<br>(4) | $\tau$ ( $p$ -value)<br>(5) | $\sigma_{\text{obs}}$<br>(6) | $\sigma_{\text{int}}$<br>(7) | $\alpha$<br>(8)           | $\beta$<br>(9)            | $\gamma$<br>(10)          |
|---------------|---------------|------------|-----------------------------|-----------------------------|------------------------------|------------------------------|---------------------------|---------------------------|---------------------------|
| All           | LS            | 232        | 0.90 ( $<10^{-5}$ )         | 0.42 ( $<10^{-5}$ )         |                              | -                            | $0.44 \pm 0.01$           | $1.01 \pm 0.01$           |                           |
| All           | Bayesian      | 232        | $0.918_{-0.012}^{+0.010}$   |                             | 0.38                         | $0.350_{-0.018}^{+0.020}$    | $0.302_{-0.025}^{+0.026}$ | $0.986_{-0.030}^{+0.030}$ | $2.003_{-0.113}^{+0.120}$ |
| Type 1        | LS            | 137        | 0.88 ( $<0.0013$ )          | 0.40 ( $<10^{-5}$ )         |                              | -                            | $0.52 \pm 0.01$           | $0.89 \pm 0.01$           |                           |
| Type 1        | Bayesian      | 137        | $0.904_{-0.020}^{+0.017}$   |                             | 0.40                         | $0.353_{-0.022}^{+0.028}$    | $0.377_{-0.034}^{+0.033}$ | $0.941_{-0.041}^{+0.042}$ | $2.372_{-0.175}^{+0.197}$ |
| Type 2        | LS            | 95         | 0.88 ( $<10^{-5}$ )         | 0.45 ( $<10^{-5}$ )         |                              | -                            | $0.24 \pm 0.01$           | $1.00 \pm 0.01$           |                           |
| Type 2        | Bayesian      | 95         | $0.889_{-0.027}^{+0.023}$   |                             | 0.40                         | $0.325_{-0.027}^{+0.031}$    | $0.180_{-0.047}^{+0.048}$ | $0.926_{-0.059}^{+0.058}$ | $1.513_{-0.158}^{+0.180}$ |

*Notes.* Column 1: sample; Column 2: linear regression technique. LS: least squares; Column 3: number of objects; Column 4: linear correlation coefficient. For least squares the Spearman's rank and the associated probability that the correlation is entirely caused by distance based on our Monte Carlo simulations; Column 5: Kendall's partial correlation coefficient and probability that the correlation is entirely caused by distance based on our Monte Carlo simulations; Column 6: observed scatter in  $L_{6\mu\text{m}}$  about the regression line; Column 7: intrinsic scatter about the regression line. At a given X-ray luminosity,  $\sigma_{\text{int}}$  denotes the standard deviation in the mid-IR luminosity; Columns 8 and 9: intercept and slope of the regression, respectively (Equation 1); Column 10: constant in linear space (Equation 2). Uncertainties are  $1\sigma$ .

AGN with  $L_{2-10\text{keV}}$  in the range  $10^{42}$ - $10^{43}\text{erg s}^{-1}$  and for  $>99$  per cent of the sources with  $L_{2-10\text{keV}} \geq 10^{43}\text{erg s}^{-1}$ .

If we assume instead that the hosts of our AGN with  $z > 0.5$  are Ultraluminous Infrared Galaxies (ULIRGs) with  $L_{8-1000\mu\text{m}} \leq 6 \times 10^{12} L_{\odot}$  (very IR-luminous galaxies become more numerous at high  $z$ ), and SFRs  $\sim 1000 M_{\odot}\text{yr}^{-1}$ , we find that the contamination from star formation at rest-frame  $6\mu\text{m}$  is less than 15 per cent for 89.1 per cent of these sources. Table 2 lists our (very conservative) median upper limits on the level of contamination from star formation at rest-frame  $6\mu\text{m}$  as a function of AGN class and luminosity.

For comparison, the median upper limit on the star formation contamination to the *WISE*  $12\mu\text{m}$  passband is 18 per cent at AGN luminosities  $10^{42} < L_{2-10\text{keV}} < 10^{43}\text{erg s}^{-1}$ , and less than 4 per cent at higher luminosities. At the rest-frame wavelengths sampled with the *WISE*  $3.4$  and  $4.6\mu\text{m}$  passbands the contamination from star formation should be negligible.

We note that to compute the above numbers we have used the full sample of objects i.e., including those for which we have only upper limits on their  $22\mu\text{m}$  fluxes. From the comparison of the  $12\mu\text{m}$  flux distributions and ( $f_{22}/f_{12}$ ) IR flux ratios (using  $1\sigma$  upper limits for  $f_{22}$  if not detected), we have found that the objects in BUXS that have escaped detection at  $22\mu\text{m}$  are  $\sim 4$ - $5$  times fainter at  $12\mu\text{m}$  than those detected at  $22\mu\text{m}$ , but they also have on average lower ( $\sim 0.8$ - $0.9$  times smaller) IR flux ratios. This implies even lower levels of contamination from dust in star forming regions in the objects not detected with *WISE* at  $22\mu\text{m}$ .

### 3.4 Reliability of rest-frame $6\mu\text{m}$ luminosities for $z > 1$ AGN

It is well known that there is some curvature in the IR continuum emission of AGN at rest-frame wavelengths close to the  $\sim 1\mu\text{m}$  inflection point between the UV and near-IR bumps (Elvis et al. 1994; Richards et al. 2006). This means that our linear interpolation/extrapolation approach, based on the *WISE* fluxes at  $4.6$  and  $12\mu\text{m}$ , might be overestimating the  $6\mu\text{m}$  luminosities for objects at  $z > 1$ , when the *WISE*  $4.6\mu\text{m}$  band is sampling rest-frame wavelengths

$\lesssim 2\mu\text{m}$ . To investigate such effect we have compared our derived  $6\mu\text{m}$  luminosities with those obtained using the *WISE* fluxes at  $12$  and  $22\mu\text{m}$ . We have used for this comparison all AGN in BUXS with  $z > 1$  and detection with  $\text{SNR} \geq 2$  at  $22\mu\text{m}$  (19 out of 37 objects with  $z > 1$ ). We have found a median (mean) difference in the logarithm of the  $6\mu\text{m}$  luminosities of just  $-0.02$  ( $-0.02$ ). Although the numbers involved in the comparison are small, these results show that at up to  $z \sim 2$ , rest-frame  $6\mu\text{m}$  AGN luminosities can be robustly determined using the *WISE*  $4.6$  and  $12\mu\text{m}$  fluxes alone. In addition, we confirm that contamination from dust emission in star forming regions to the *WISE*  $22\mu\text{m}$  fluxes is not important.

## 4 CORRELATION OF $L_{6\mu\text{m}}$ AND $L_{2-10\text{keV}}$ LUMINOSITIES

### 4.1 Linear regression technique

From now on, we will refer to the mid-IR monochromatic luminosities at rest-frame  $6\mu\text{m}$  as  $L_{6\mu\text{m}}$  while  $L_{2-10\text{keV}}$  are the rest-frame 2-10 keV X-ray luminosities corrected for X-ray absorption (see Sec. 2.3). To determine the relationship between  $L_{6\mu\text{m}}$  and  $L_{2-10\text{keV}}$  we have performed a linear regression in log-log space using two different approaches: the least squares  $\chi^2$  minimization (Press et al. 1992) and the Bayesian maximum likelihood method proposed by Kelly (2007, hereafter K07)<sup>6</sup>. For the K07 technique the data are fitted using the Metropolis-Hastings Markov Chain Monte Carlo (MCMC) algorithm sampler. We have adopted uniform prior distributions for the regression parameters. The best-fit parameters and their corresponding uncertainties have been determined by taking the median and the 16 and 84 percentiles (68 per cent enclosed, equivalent to  $1\sigma$ ) from the posterior probability distributions of the model parameters using  $10^4$  iterations from the MCMC sampler. The two regression techniques account for measurement errors in both the independent and dependent variables. However,

<sup>6</sup> [http://idlastro.gsfc.nasa.gov/ftp/pro/math/linmix\\_err.pro](http://idlastro.gsfc.nasa.gov/ftp/pro/math/linmix_err.pro)

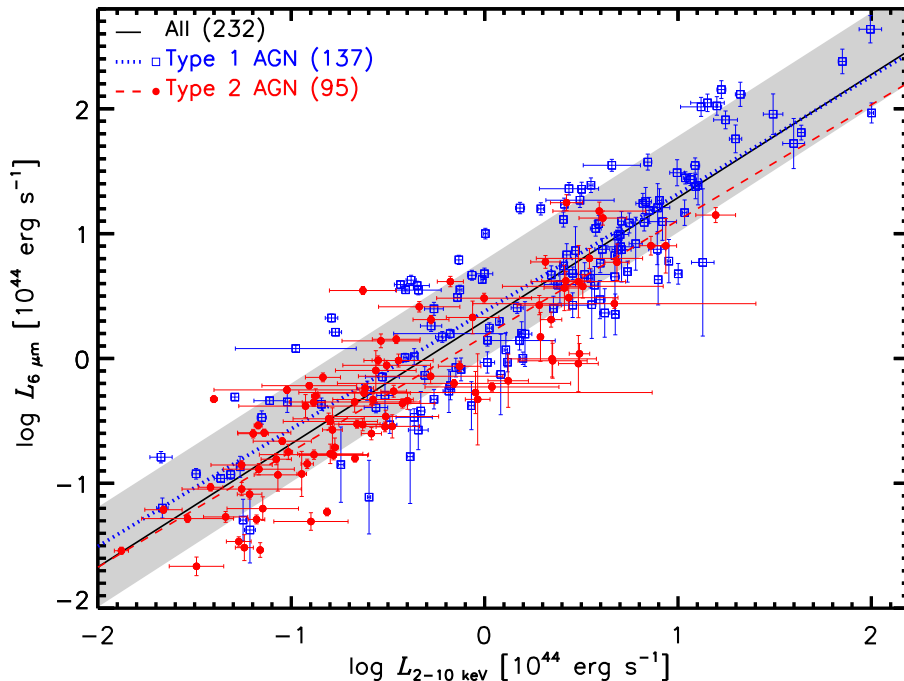


**Figure 5.** Rest-frame  $6\ \mu\text{m}$  monochromatic luminosities against 2-10 keV intrinsic (i.e., corrected for absorption) X-ray luminosities. The  $6\ \mu\text{m}$  luminosities have been corrected for the accretion disk emission and contamination from the AGN host galaxies as indicated in Sec. 3. The best-fit linear relations in log-log space derived with the K07 Bayesian approach for the full sample and the type 1 and type 2 AGN are indicated with solid, dotted and dashed lines, respectively. We compare our results with the relation derived for type 1 AGN by Lutz et al. (2004) (grey shading).

since the K07 approach determines simultaneously both the regression parameters and the intrinsic scatter<sup>7</sup>, it should provide more reliable estimates of the parameters, their associated uncertainties and of the strength of the linear correlation. Therefore, from now on we will refer to the results obtained with the K07 technique, but present those obtained from the least squares technique for comparison with results in the literature.

The linear regression techniques used here assume that the measurement errors are Gaussian. However, this is not the case for either the X-ray luminosity measurements or the uncertainties associated with the correction of the mid-IR luminosities for the accretion disk and starlight emission. To overcome this problem, for each data point with luminosity  $L$  and associated uncertainties  $L^-$  and  $L^+$  (all values in logarithmic units) we have computed a Gaussian function with mean  $L$  and dispersion  $\sigma$  such that its integral from  $L-L^-$  to  $L+L^+$  is equal to the enclosed probability given by the fits (68.3 per cent for the X-ray luminosity uncertainties and 95.4 per cent for the mid-IR luminosity uncertainties derived from SEABASs). We have used the  $1\sigma$  uncertainties derived in this way in our regression analysis.

To determine the  $L_{6\ \mu\text{m}}-L_{2-10\ \text{keV}}$  relationship we have conducted the linear regression analysis treating  $L_{2-10\ \text{keV}}$  as the independent variable and  $L_{6\ \mu\text{m}}$  as the dependent vari-

able. Our decision is based on the fact that hard X-rays, produced at distances much closer to the central SMBH (sub-parsec scales), are a more direct tracer of the AGN intrinsic power than the mid-IR emission, originating from the dusty torus at tens of parsec scales<sup>8</sup>. We have assumed a linear relation of the form:

$$\log\left(\frac{L_{6\ \mu\text{m}}}{10^{44}}\right) = \alpha + \beta \times \log\left(\frac{L_{2-10\ \text{keV}}}{10^{44}}\right) \quad (1)$$

where the luminosities are in units of  $\text{erg s}^{-1}$  and  $\alpha$  and  $\beta$  are the correlation parameters. The luminosities have been nor-

<sup>7</sup> If  $x$  and  $y$  are the independent and dependent variables, respectively, the scatter in  $y$  at fixed  $x$  that would have been measured if there were no errors in  $y$ .

<sup>8</sup> From a statistical point of view we note that, in the presence of intrinsic scatter, the best-fit slopes of forward and inverse regressions (i.e., switching the dependent and independent variables) can be very different. To circumvent such problem both variables are often treated symmetrically using the bisector line (e.g. Isobe et al. 1990). However, if the dependent variable of the linear regression analysis depends on the parameter used to select the sample (although our AGN sample is X-ray flux limited we stress that we are only using objects from BUXS with  $L_{2-10\ \text{keV}} > 10^{42}\ \text{erg s}^{-1}$ ), the truncation of the data set will artificially flatten the measured slope due to the increased loss of objects with low X-ray luminosities at low mid-IR luminosities (Kelly 2007). Thus, the conventional forward fit relation i.e., fitting  $L_{6\ \mu\text{m}}$  at a given  $L_{2-10\ \text{keV}}$ , should provide the more accurate estimate of the existing relationship between the mid-IR and X-ray luminosities for our AGN.

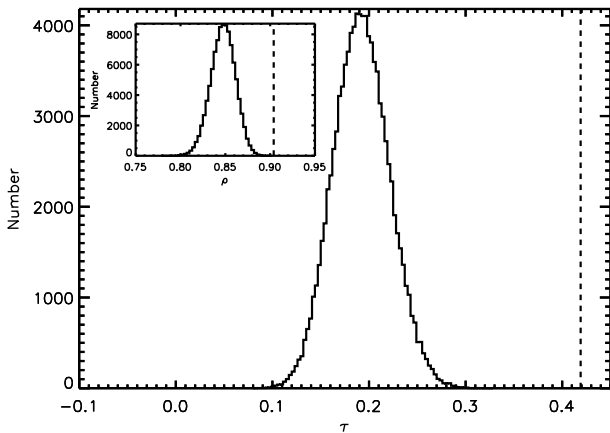


**Figure 6.** Results of the Monte Carlo simulations conducted to determine the correlation between  $L_{6\mu\text{m}}$  and  $L_{2-10\text{keV}}$  (solid histograms). The large histogram represents the distribution of the Kendall partial correlation coefficient (where distance effects have been taken into account) while the inset plot illustrates the results for the Spearman correlation coefficient. The vertical dashed lines represent the correlation coefficients obtained for the original sample.

malized at  $L_{2-10\text{keV}}=10^{44}\text{ergs}^{-1}$ , roughly the mean AGN power of our sample.

Equation 1 can be written as

$$\left(\frac{L_{6\mu\text{m}}}{10^{44}}\right) = \gamma \times \left(\frac{L_{2-10\text{keV}}}{10^{44}}\right)^\beta \quad (2)$$

where we have computed  $\gamma$  ( $\sim 10^\alpha$ ) and its  $1\sigma$  uncertainties as the median and the 16 and 84 percentiles of the probability density distributions of  $\gamma$ . The latter were computed with a Monte Carlo sampling of the posterior probability distributions of  $\alpha$ .

#### 4.2 The $L_{6\mu\text{m}}-L_{2-10\text{keV}}$ relation

Table 3 summarizes the results of our regression analysis. The best-fit linear relations for the full sample and the type 1 and type 2 AGN obtained with the K07 technique are illustrated in Fig. 5. Table A1 lists the X-ray and  $6\mu\text{m}$  luminosities of our AGN.

Although the K07 technique determines the strength of the correlation between  $L_{6\mu\text{m}}$  and  $L_{2-10\text{keV}}$ , we have also computed the Spearman rank-order correlation coefficient ( $\rho$ ) for comparison. Both the Spearman's rank and the Bayesian correlation coefficients confirm the tight correlation between mid-IR and X-ray luminosities over more than three decades in AGN luminosity (from  $10^{42} - 10^{46}\text{ergs}^{-1}$ ).

To investigate the role of distance in our luminosity-luminosity correlation, we have also performed a partial Kendall  $\tau$  correlation test taking into account the common dependence of  $L_{6\mu\text{m}}$  and  $L_{2-10\text{keV}}$  on the distance. To compute the significance of the measured Spearman  $\rho$  and Kendall  $\tau$  correlation coefficients for our sample we have conducted a "scrambling test" (e.g. Merloni et al. 2006; Bianchi et al. 2009). The idea behind this test is as follows: for each source we keep its X-ray luminosity and  $z$ . We then

assign them  $6\mu\text{m}$  fluxes from the sample at random with replacement (bootstrap) and they are converted to a mid-IR luminosity using the  $z$  of the source. In this way we are removing any intrinsic correlation between  $L_{6\mu\text{m}}$  and  $L_{2-10\text{keV}}$  that is not associated to distance effects. We have repeated this Monte Carlo test  $10^5$  times calculating each time the Spearman  $\rho$  and Kendall  $\tau$  correlation coefficients. The simulations were conducted for both the full sample and for the type 1 and type 2 AGN samples. The results are listed in Table 3 and are illustrated in Fig. 6 for the full sample (similar results were obtained for the type 1 and type 2 AGN). The values of the correlation coefficients obtained for the original dataset are well above the distribution of those for the simulated samples. Our analysis shows that the probability that the measured correlation between  $L_{6\mu\text{m}}$  and  $L_{2-10\text{keV}}$  is entirely due to the range of distances in our sample is almost always  $<10^{-5}$  (see Table 3).

At a given X-ray luminosity, the standard deviation in  $6\mu\text{m}$  luminosities is very similar for both type 1 ( $\sim 0.353$  dex) and type 2 ( $\sim 0.325$  dex) AGN and the slopes of the linear regression relations are compatible, within the uncertainties. Despite this, type 1 AGN are overall  $\sim 1.3-2$  times brighter than type 2 AGN at  $6\mu\text{m}$  at a given X-ray luminosity, albeit with a large overlap between both populations.

The shaded area in Fig. 5 shows the relation (and  $1\sigma$  dispersion) for type 1 AGN from Lutz et al. (2004). We have compared the mid-IR/X-ray luminosity ratio distributions of our AGN and the 42 objects in Lutz et al. (2004) with  $L_{2-10\text{keV}} > 10^{42}\text{ergs}^{-1}$ , detections at  $6\mu\text{m}$  and estimates of the intrinsic X-ray luminosity. According to the two-sample Kolmogorov-Smirnov (KS) test, the probability of rejecting the null hypothesis (the two samples are drawn from the same parent population) is 61.3 per cent. We can therefore conclude that the two distributions are consistent with each other. We have also compared the  $L_{12\mu\text{m}}/L_{2-10\text{keV}}$  luminosity ratio distributions of our AGN and those from Gandhi et al. (2009) with X-ray luminosities  $> 10^{42}\text{ergs}^{-1}$  (37 AGN), where  $L_{12\mu\text{m}}$  are the monochromatic luminosities in  $\nu L_\nu$  units at rest-frame  $12\mu\text{m}$ . To do the comparison we computed  $L_{12\mu\text{m}}$  (corrected for the accretion disk emission and contamination from the AGN host galaxies) for each of our AGN as indicated in Sec. 3. According to the KS test, the distributions of  $L_{12\mu\text{m}}/L_{2-10\text{keV}}$  are consistent with each other (47.3 per cent probability of rejecting the null hypothesis). Therefore our results are compatible with published mid-IR:X-ray relations for local AGN (e.g. Krabbe, Böker, & Maiolino 2001; Lutz et al. 2004; Gandhi et al. 2009; Levenson et al. 2009; Asmus et al. 2014). Nonetheless, they do not support the luminosity-dependent relationship derived for the type 1 AGN in the Chandra COSMOS (C-COSMOS) and Chandra Deep Field South (CDFs) surveys suggested by Fiore et al. (2009).

We have demonstrated that at AGN luminosities  $L_{2-10\text{keV}} > 10^{42}\text{ergs}^{-1}$ , the mid-IR emission detected with *WISE* at rest-frame wavelengths  $\sim 6\mu\text{m}$  is dominated by hot dust heated by the AGN. Therefore it is possible to indirectly infer the intrinsic 2-10 keV X-ray luminosities of AGN with data from *WISE* by inverting Equation 1 and Equation 2 after correcting the  $6\mu\text{m}$  luminosities for contamination from the AGN hosts and the accretion disk. Moreover, we have shown that such corrections are not negligible, at a  $\sim 30$  per cent level for AGN with

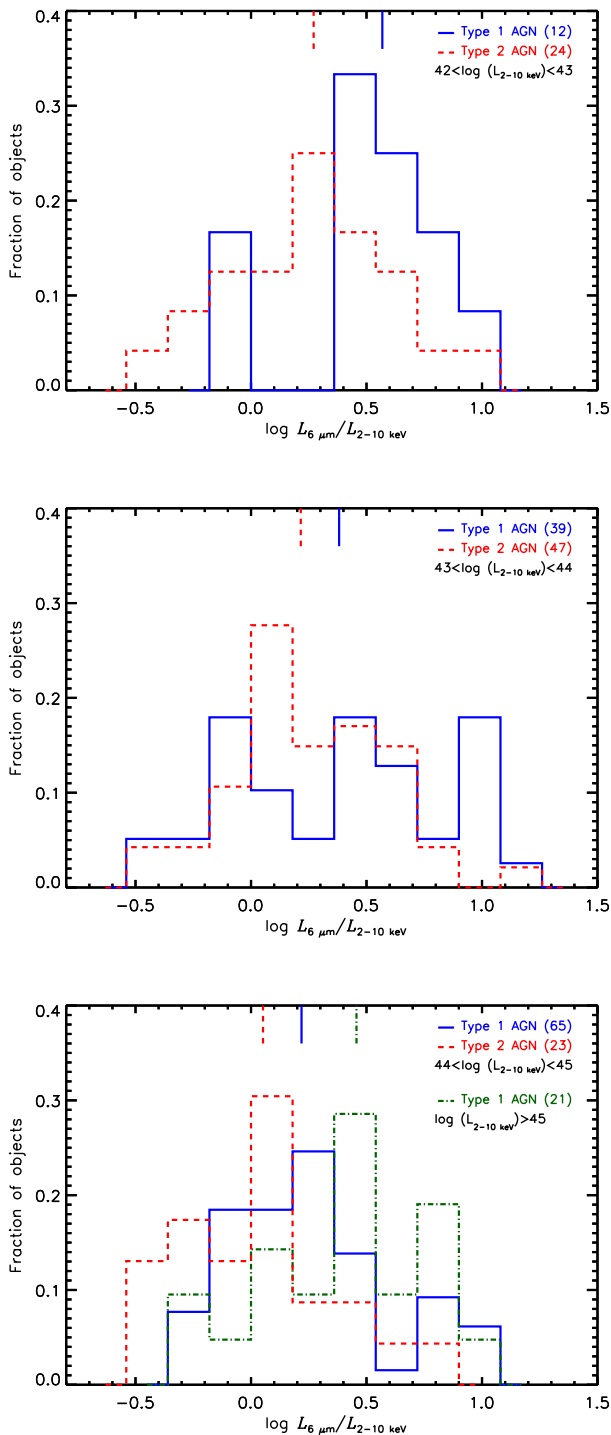


**Figure 7.** Distribution of  $6\ \mu\text{m}$  to X-ray luminosity ratios (in logarithmic units). The vertical lines at the top of the figure indicate the median values of the distributions. The bottom plot also shows the distribution (and its median) for the type 1 AGN with  $L_{2-10\ \text{keV}} > 10^{45}\ \text{erg s}^{-1}$

$10^{42} < L_{2-10\ \text{keV}} < 10^{43}\ \text{erg s}^{-1}$  and at a  $\sim 12$ - $18$  per cent level for AGN with  $10^{43} < L_{2-10\ \text{keV}} < 10^{46}\ \text{erg s}^{-1}$ . Based on the full sample, X-ray luminosities can be determined with a root mean square (rms) error of  $0.376$  dex. The corresponding rms values for type 1 and type 2 AGN are  $0.404$  dex and  $0.355$  dex, respectively<sup>9</sup>.

## 5 DISCUSSION

### 5.1 Dispersion of the $L_{6\ \mu\text{m}}-L_{2-10\ \text{keV}}$ relation

Several factors can contribute to the measured scatter of the  $L_{6\ \mu\text{m}}$  versus  $L_{2-10\ \text{keV}}$  relationship, such as the inherent large dispersion in the individual SED shapes associated with the varying properties of the material responsible for the X-ray and mid-IR emission and AGN variability effects (the X-ray and mid-IR observations have been taken several years apart). As X-rays are produced in a compact region close to the central SMBH, they trace more directly changes in the AGN bolometric radiative output than the mid-IR.

AGN torus models with both smooth and clumpy dust distributions predict anisotropic dust emission at rest-frame  $6\ \mu\text{m}$  (e.g. Pier & Krolik 1992; Fritz, Franceschini, & Hatziminaoglou 2006; Nenkova et al. 2008a, 2008b). Although smooth-density models typically predict higher levels of mid-IR anisotropy (e.g.  $\sim$ an order of magnitude from face-on to edge-on views at rest-frame  $6\ \mu\text{m}$ ; Pier & Krolik 1992) it has recently been shown that the anisotropy level depends mainly on the model assumptions and not so much on the adopted dust morphology (i.e., smooth or clumpy; Feltre et al. 2012). Nevertheless, if the mid-IR emission is not isotropic at the rest-frame wavelengths involved in our study, such effect should contribute to the measured intrinsic dispersion in the  $L_{6\ \mu\text{m}}$  versus  $L_{2-10\ \text{keV}}$  relationship.

We note that, if contamination from star formation were the main contributor to the observed spread, this would imply a contamination to the  $6\ \mu\text{m}$  luminosities greater than  $1 \cdot 10^{-\sigma_{\text{int}}} \sim 56$  per cent on average. This is unlikely to be the case as demonstrated in Sec. 3.3. Moreover, as our sample consists of AGN with absorption in the Compton-thin regime, uncertainties associated with the correction of the X-ray luminosities for intrinsic X-ray absorption are generally small given the good quality X-ray spectroscopic data available for all sources. This is supported by the fact that the intrinsic spread of  $L_{6\ \mu\text{m}}$  at a given  $L_{2-10\ \text{keV}}$  is comparable for (mostly unabsorbed) type 1 and (highly absorbed) type 2 AGN.

### 5.2 A luminosity-independent dusty torus?

Several works in the literature claim that the fraction of AGN bolometric luminosity that is reprocessed in the mid-IR increases at a lower rate than the AGN intrinsic bolometric power (e.g. Barcons et al. 1995; Maiolino et al. 2007; Treister, Krolik, & Dullemond

<sup>9</sup> To determine the rms we have used the  $6\ \mu\text{m}$  luminosity range where we can compute the dispersion in X-ray luminosities,  $\log L_{6\ \mu\text{m}} > 42.7\ \text{erg s}^{-1}$  for the full sample and type 2 AGN and  $\log L_{6\ \mu\text{m}} > 42.8\ \text{erg s}^{-1}$  for type 1 AGN.



**Table 4.** Summary of the properties of the distributions of rest-frame  $6\mu\text{m}$  over 2-10 keV luminosities.

| $\Delta\log(L_{2-10\text{ keV}})$<br>erg s <sup>-1</sup> | $N^{\text{type 1}}$ | $\log(L_{6\mu\text{m}}/L_{2-10\text{ keV}})^{\text{type 1}}$ |                        | $N^{\text{type 2}}$ | $\log(L_{6\mu\text{m}}/L_{2-10\text{ keV}})^{\text{type 2}}$ |                        |
|--|---------------------|--|------------------------|---------------------|--|------------------------|
|  |                     | Mean   | Median                 |                     | Mean   | Median                 |
| (1)  | (2)                 | (3)  | (4)                    | (5)                 | (6)  | (7)                    |
| 42-45  | 116                 | $0.33 \pm 0.40$  | $0.31^{+0.51}_{-0.38}$ | 94                  | $0.20 \pm 0.36$  | $0.15^{+0.42}_{-0.33}$ |
| 42-43  | 12                  | $0.50 \pm 0.36$  | $0.57^{+0.31}_{-0.61}$ | 24                  | $0.25 \pm 0.35$  | $0.27^{+0.32}_{-0.44}$ |
| 43-44  | 39                  | $0.38 \pm 0.47$  | $0.38^{+0.55}_{-0.47}$ | 47                  | $0.25 \pm 0.34$  | $0.21^{+0.37}_{-0.25}$ |
| 44-45  | 65                  | $0.26 \pm 0.34$  | $0.22^{+0.49}_{-0.26}$ | 23                  | $0.04 \pm 0.36$  | $0.05^{+0.41}_{-0.40}$ |
| 45-46  | 21                  | $0.41 \pm 0.38$  | $0.46^{+0.37}_{-0.33}$ | 1                   | -  | -                      |

*Notes.* Column 1: X-ray luminosity interval; Column 2: number of type 1 AGN in the sample; Columns 3 and 4: mean and median of the distribution of the mid-IR/X-ray luminosity ratios for type 1 AGN, respectively. Column 5: number of type 2 AGN in the sample; Columns 6 and 7: mean and median of the distribution of the mid-IR/X-ray luminosity ratios for type 2 AGN. The quoted errors in Columns 3 and 6 are the  $1\sigma$  dispersion of the distributions while the errors in Columns 4 and 7 correspond to the 16 and 84 percentiles.

2008; McKernan et al. 2009; Mor, Netzer, & Elitzur 2009; Calderone, Sbarrato, & Ghisellini 2012). These results have been interpreted in terms of a luminosity-dependent unification model, where the properties of the AGN dusty torus, such as the geometrical covering factor, vary with luminosity (e.g. Lawrence 1991; Simpson 2005; Della Ceca et al. 2008). Other studies find, however, either weak or no luminosity dependence (Gandhi et al. 2009; Levenson et al. 2009; Roseboom et al. 2013).

We have determined a relationship between  $L_{6\mu\text{m}}$  and  $L_{2-10\text{ keV}}$  for both type 1 and type 2 AGN that is consistent with being linear. Furthermore, the average rate of change of  $L_{6\mu\text{m}}$  with respect to  $L_{2-10\text{ keV}}$  is similar in the two AGN classes. Fig. 7 shows the distributions of  $\log(L_{6\mu\text{m}}/L_{2-10\text{ keV}})$  for type 1 and type 2 AGN at different X-ray luminosities. Table 4 lists the mean and median of these distributions. We find a mild variation, if at all, of  $\log(L_{6\mu\text{m}}/L_{2-10\text{ keV}})$  with luminosity, in any case well within the mutual dispersions.

In this comparison we are implicitly assuming that the 2-10 keV intrinsic luminosity is a reliable proxy for the AGN bolometric radiative power and that the hard X-ray bolometric correction is constant across the luminosity range of our sample. Recent works in the literature suggest that the X-ray emission of AGN is likely weakly anisotropic, in the sense that type 2 AGN appear intrinsically fainter than type 1 AGN at X-ray energies (e.g. Diamond-Stanic, Rieke, & Rigby 2009; LaMassa et al. 2010; Dicken et al. 2014; Liu et al. 2014 and references therein). If this was the case, this should have no effect on the results obtained for our type 1 AGN. On the other hand, taking into account that the amplitude of the X-ray anisotropy does not seem to vary with luminosity (Liu et al. 2014) a correction for X-ray anisotropy effects would move the points for the type 2 AGN in Fig. 5 to the right but, should not change significantly the slope of the correlation between their mid-IR and X-ray luminosities.

We note that, if the X-ray bolometric correction increases with AGN luminosity then the power-law spectral slope of the equivalent relation between  $L_{6\mu\text{m}}$  and the bolometric luminosity  $L_{\text{bol}}$  would decrease. If we adopt, for example, the luminosity-dependent bolometric correction of Marconi et al. (2004), we would obtain  $L_{6\mu\text{m}} \propto L_{\text{bol}}^{0.750 \pm 0.024}$  for the full sample of objects (for a similar luminosity-dependence of the hard X-ray bolometric correction see also

Hopkins, Richards, & Hernquist 2007). More recent studies in the literature suggest, however, a much weaker dependence of the hard X-ray bolometric correction with AGN luminosity if any (Vasudevan & Fabian 2007; Marchese et al. 2012; Fanali et al. 2013).

Finally, we do not expect our results to be affected by sample selection biases. On the one hand, as indicated in Sec. 2.2, only six sources in BUXS do not have detections in ALLWISE with SNR above our detection threshold. Hence, our AGN sample is not biased against infrared-faint sources (these sources would occupy the lower right corner in Fig. 5). On the other hand, spectroscopic follow-up studies of infrared selected AGN candidates did not find evidence for the existence of a population of AGN with infrared-to-X-ray luminosity ratios significantly higher than those of the AGN revealed in X-ray surveys, at least not for AGN with X-ray luminosities and  $z$  in the range sampled with the BUXS survey (e.g. Lacy et al. 2013).

Thus, our study shows that, if the fraction of AGN bolometric luminosity that is reprocessed in the mid-IR decreases with the AGN luminosity, the effect is certainly weak in both type 1 and type 2 AGN over the three decades in X-ray luminosity covered with our sample. This finding is at odds with simple receding torus models (e.g. Simpson 2005).

### 5.3 Anisotropy of the AGN emission at $6\mu\text{m}$

In Sec. 4.2 we have shown that at a given X-ray luminosity, X-ray selected type 1 AGN are on average  $\sim 1.3$ -2 times more luminous at rest-frame wavelengths  $\sim 6\mu\text{m}$  than type 2 AGN although with a considerable overlap (see e.g. Ramos Almeida et al. 2007, Hönig et al. 2011 and Yang, Wang, & Liu 2014 for similar results). A KS test gives a probability of 2.4 per cent that the distributions of  $\log(L_{6\mu\text{m}}/L_{2-10\text{ keV}})$  for type 1 and type 2 AGN are drawn from the same sample. As pointed out in Sec. 5.2, the AGN X-ray emission is likely weakly anisotropic. If this is the case, a correction for such effect would make the  $6\mu\text{m}$ -to-X-ray luminosity ratios smaller for type 2 AGN and thus the differences in mid-IR luminosities at a given X-ray luminosity between type 1 and type 2 AGN would be even larger than our estimation. To better understand this effect we show in Fig. 8 the median rest-frame UV-to-mid-IR SEDs of our AGN in three X-ray luminosity bins before applying any correction for host galaxy contamination. These were computed

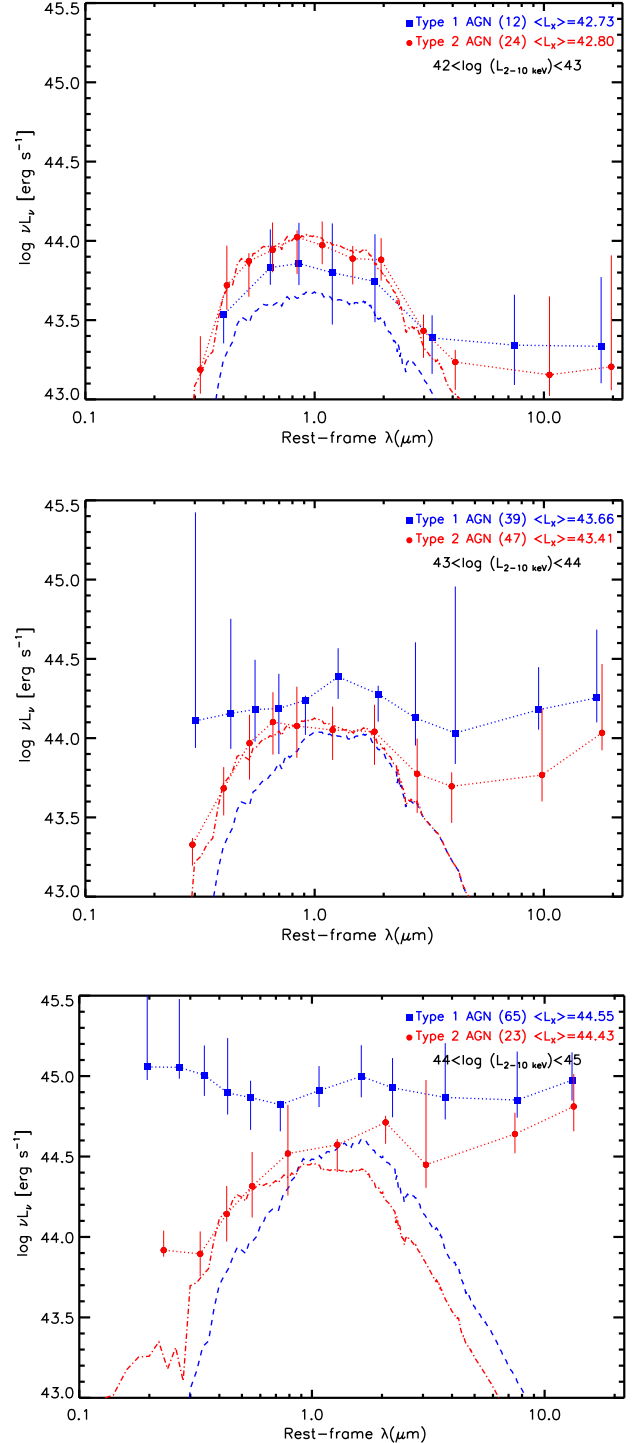
by first shifting the individual SEDs to a common rest-frame wavelength grid. We then converted the fluxes to luminosities in  $\nu L_\nu$  units and we combined them in wavelength bins containing at least 15 points. Each value represents the median of the points in the bin while the dispersion is defined with the 16 and 84 percentiles. We did not take into account upper-limits in the computation of the median SEDs hence, as not all AGN were detected with *WISE* at  $22\ \mu\text{m}$ , our median SEDs might be somewhat redder than they should at the longest wavelengths ( $>10\ \mu\text{m}$ ).

Fig. 8 also shows the median SEDs of the best-fit host galaxy stellar emission templates. Although a description of the properties of the host galaxies of our AGN is beyond the scope of this paper, we see that on average there are no significant differences in the near-IR luminosities of the type 1 and type 2 AGN hosts (a proxy for their stellar masses) except at luminosities  $10^{42} - 10^{43}\ \text{erg s}^{-1}$ . We note, however, that the results obtained at these luminosities should be treated with caution. The number of type 1 AGN is rather small and hence the sample might not be representative of the overall population. Furthermore, at X-ray luminosities from  $10^{42}$  to  $10^{43}\ \text{erg s}^{-1}$ , the emission from the host galaxies could dilute the AGN signatures in a significant fraction of objects (50 per cent; see Fig. 5 in Caccianiga et al. 2007). Hence, it is likely that at  $L_{2-10\ \text{keV}} < 10^{43}\ \text{erg s}^{-1}$  some type 1 AGN in BUXS might have been misclassified as type 2 AGN.

The dispersion in the bins illustrated in Fig. 8 reflects not only changes in the intrinsic continuum shape of the different SED components between objects but also the varying levels of host galaxy contamination and the dispersion in AGN luminosities. Fig. 8 shows that, even after accounting for the small differences in X-ray luminosities between type 1 and type 2 AGN in the bins, type 2 AGN are overall fainter sources at rest-frame wavelengths  $\gtrsim 4\ \mu\text{m}$  out to at least  $12\ \mu\text{m}$  than type 1 AGN at a given X-ray luminosity.

To investigate in more detail whether the observed continuum shape of the mid-IR emission associated to the dusty torus in type 1 and type 2 AGN is different we have compared the distributions of the  $(L_{6\ \mu\text{m}}/L_{12\ \mu\text{m}})$  luminosity ratios for the two AGN classes. The  $12\ \mu\text{m}$  luminosities were determined using linear extrapolation in log-log space between the *WISE* catalogued fluxes at  $4.6$  and  $12\ \mu\text{m}$  and were corrected for both the accretion disk emission and contamination from the AGN host galaxies. The results are presented in Fig. 9. Clearly, the mid-IR continuum of type 2 AGN is on average redder<sup>10</sup> than for type 1 AGN, albeit with a large overlap between both populations. According to the KS test, the probability of rejecting the null hypothesis (the two samples are drawn from the same parent population) is higher than 99.99 per cent. We note that if we use instead the observed  $L_{6\ \mu\text{m}}$  and  $L_{12\ \mu\text{m}}$  luminosities (i.e., without any correction for contamination) we still find a probability of rejecting the null hypothesis of 99.6 per cent. We have not found any significant dependence of  $\log(L_{6\ \mu\text{m}}/L_{12\ \mu\text{m}})$  on luminosity in either type 1 or type 2 AGN. Furthermore, if we split the sample into luminosity bins as in Fig. 8, we still can reject

<sup>10</sup> The term red (blue) refers to increasing (decreasing) fluxes in  $\nu f_\nu$  at longer wavelengths.



**Figure 8.** Rest-frame median SEDs of the type 1 and type 2 AGN (filled symbols) in three intervals of AGN luminosity before correction for host galaxy emission. In the plots are also indicated the mean X-ray luminosities of each sub-sample. To help guide the eye the points are connected with a power law in linear space (dotted lines). The dashed and dotted-dashed lines represent the median of the best-fit SEDs of the host galaxies. The vertical error bars indicate the 16 and 84 percentiles (68 per cent enclosed, equivalent to  $1\sigma$ ) of the distribution of values.

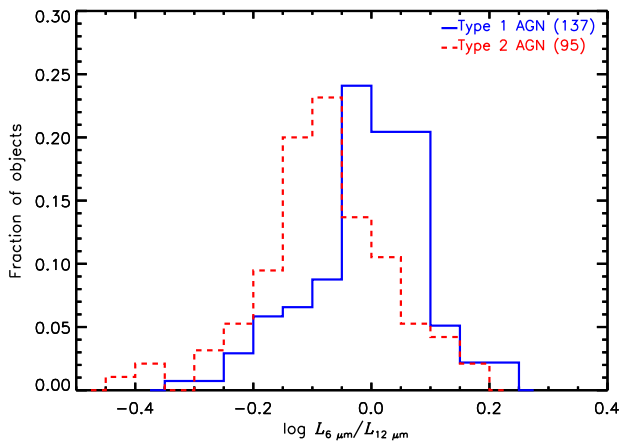


**Figure 9.** Distributions of the rest-frame  $6\mu\text{m}$  versus  $12\mu\text{m}$  mid-IR luminosity ratios for type 1 and type 2 AGN (in logarithmic units). The mid-IR luminosities have been corrected for the accretion disk emission and contamination from the AGN host galaxies.

the null hypothesis probability (i.e. that the distributions of  $\log(L_{6\mu\text{m}}/L_{12\mu\text{m}})$  for type 1 and type 2 AGN are drawn from the same parent population) with a confidence of 99.7 and 99.98 per cent for objects with  $10^{43} < L_{2-10\text{keV}} < 10^{44} \text{ erg s}^{-1}$  and  $10^{44} < L_{2-10\text{keV}} < 10^{45} \text{ erg s}^{-1}$ , respectively. Using the KS test, we cannot reject the null hypothesis for objects with  $L_{2-10\text{keV}} < 10^{43} \text{ erg s}^{-1}$ , most likely due to the issues indicated previously.

Our results are in agreement with previous studies of the mid-IR SEDs of local Seyfert galaxies (e.g. Alonso-Herrero et al. 2003; Ramos Almeida et al. 2011 and references therein) and luminous quasars at intermediate  $z$  (e.g. Hernán-Caballero et al. 2009).

#### 5.4 Dependence of the rest-frame $6\mu\text{m}$ emission on the X-ray absorption?

As expected, the UV-optical dust reddening and line-of-sight X-ray absorption properties of our AGN are highly correlated, in the sense that X-ray absorption is less common in objects classified in the UV/optical as type 1 and their X-ray column densities are on average lower than those measured for type 2 AGN (e.g. Mainieri et al. 2002; Mateos et al. 2005a, 2005b; Tozzi et al. 2006; Winter et al. 2009; Mateos et al. 2010; Corral et al. 2011; Scott et al. 2011; Merloni et al. 2014). These results have often been interpreted in terms of orientation-based unified models, where the AGN optical classification and X-ray column density are tracers of the inclination angle of the dusty torus with respect to our line-of-sight.

Our study supports the idea that there are differences in the properties of the dusty torus emission between type 1 and type 2 AGN. What is less clear is whether such emission varies strongly with the X-ray absorption. For example, the study of Silva, Maiolino, & Granato (2004) suggests that it remains nearly unchanged up to X-ray column densities approaching the Compton-thick regime but it is significantly different for Compton-thick AGN.

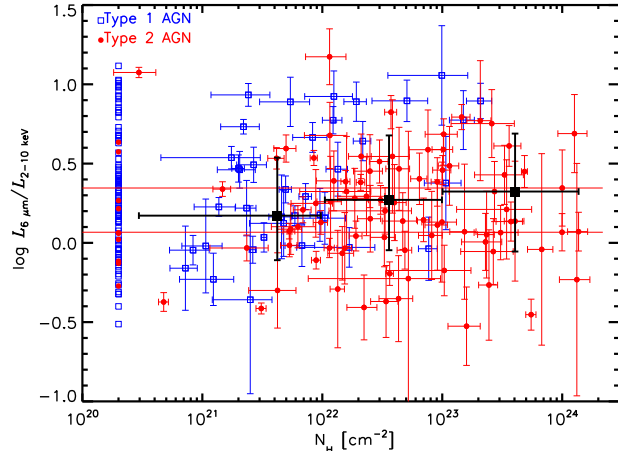


**Figure 10.** Mid-IR to X-ray luminosity ratio (in logarithmic units) versus the line-of-sight X-ray absorption. For clarity, we have arbitrarily assigned a column density of  $2 \times 10^{20} \text{ cm}^{-2}$  to the unabsorbed objects. Large filled squares and their vertical error bars are the median and 16 and 84 percentiles in different column density intervals indicated with the horizontal error bars.

To investigate whether the dusty torus emission depends on the X-ray absorption we have computed the strength of the correlation between  $\log(L_{6\mu\text{m}}/L_{2-10\text{keV}})$  and  $N_{\text{H}}$  in our sample of AGN, where  $L_{6\mu\text{m}}$  has been corrected for the emission from the accretion disk and the AGN hosts as indicated in Sec. 3.1. Based on the F-test probability at a 95 per cent confidence level 37 type 1 AGN and 85 type 2 AGN are X-ray absorbed (see Sec. 2.3 for details). The data are shown in Fig. 10. To determine the strength of the correlation between  $\log(L_{6\mu\text{m}}/L_{2-10\text{keV}})$  and  $N_{\text{H}}$  we have used the K07 technique as it takes into account both the measurement errors and intrinsic scatter. We have used the full AGN sample considering the  $1\sigma$  upper limits in  $N_{\text{H}}$  determined from the best-fit models for the X-ray unabsorbed objects.

The distributions of  $\log(L_{6\mu\text{m}}/L_{2-10\text{keV}})$  for absorbed and unabsorbed objects are indistinguishable (47.0 per cent probability to reject the null hypothesis). As pointed out before, the optical classification and X-ray absorption of our AGN are highly correlated, but the correspondence is not one-to-one. Based on the F-test probability at a 95 per cent confidence level, 37/137 (27 per cent) type 1 AGN are X-ray absorbed while 10/95 (10.5 per cent) type 2 AGN are X-ray unabsorbed. If we adopt a column density threshold of  $N_{\text{H}} = 4 \times 10^{21} \text{ cm}^{-2}$  to distinguish between X-ray unobscured and obscured AGN, as in recent studies, the numbers change to 22/137 type 1 AGN (16 per cent) and 15/95 type 2 AGN (15.8 per cent). This effect smooths out the already small difference in the  $L_{6\mu\text{m}}/L_{2-10\text{keV}}$  luminosity ratio distributions between type 1 and type 2 AGN.

Moreover, we find that the mid-IR/X-ray luminosity ratio is largely independent of the line-of-sight X-ray absorption (linear correlation coefficient  $\rho = 0.03 \pm 0.11$ ). Median values of  $\log(L_{6\mu\text{m}}/L_{2-10\text{keV}})$  are  $0.17_{-0.28}^{+0.37}$  for  $N_{\text{H}} < 10^{22} \text{ cm}^{-2}$ ,  $0.27_{-0.32}^{+0.41}$  for  $10^{22} < N_{\text{H}} < 10^{23} \text{ cm}^{-2}$  and  $0.32_{-0.38}^{+0.37}$  for  $N_{\text{H}} > 10^{23} \text{ cm}^{-2}$  (for similar results see also Lutz et al. 2004; Gandhi et al. 2009; Ichikawa et al. 2012).

This is an expected result. On the one hand, in X-rays we are measuring the amount of absorption along our line-of-sight to each AGN. Clearly, the measured absorption values could change significantly if we were observing the objects along different lines-of-sight. On the other hand, at mid-IR wavelengths we are measuring the integrated reprocessed emission from all the material in the dusty torus in the plane of the sky. If this material is absorbing the X-rays and it is re-emitting the radiation almost isotropically, we would expect to observe approximately the same  $\log(L_{6\mu\text{m}}/L_{2-10\text{keV}})$  value independently of orientation. We have shown that the AGN emission at rest-frame  $6\mu\text{m}$  is not free of dust extinction effects. Nevertheless, there is certainly a large overlap between the  $\log(L_{6\mu\text{m}}/L_{12\mu\text{m}})$  distributions for the type 1 and type 2 AGN populations ( $\sim 0.1$  dex of shift; see Fig. 9) and the scatter in the luminosity ratio distributions is significant. This makes orientation-dependent effects, such as a correlation with the line-of-sight X-ray absorption, difficult to detect, at least for AGN with X-ray absorption in the Compton-thin regime (for similar results see also Silva, Maiolino, & Granato 2004; Gandhi et al. 2009).

To summarize, our results imply that the AGN emission at rest-frame  $6\mu\text{m}$  is not completely isotropic, due to self-absorption in the dusty torus. Such interpretation is consistent with AGN torus models with both smooth and clumpy dust distributions as they all predict anisotropic dust emission at rest-frame wavelengths of  $6\mu\text{m}$  (e.g. Pier & Krolik 1992; Fritz, Franceschini, & Hatziminaoglou 2006; Nenkova et al. 2008a, 2008b). This effect could be enhanced if, as suggested by recent results in the literature for local Seyfert galaxies, the properties of the dusty tori in type 1 and type 2 objects are different (e.g. Alonso-Herrero et al. 2011; Ramos Almeida et al. 2011). In either case, our results imply that AGN surveys at rest-frame  $\sim 6\mu\text{m}$  are subject to modest dust obscuration biases.

## 6 CONCLUSIONS

We investigate whether rest-frame  $6\mu\text{m}$  mid-IR continuum luminosities associated to the dusty torus emission of AGN determined with data from the Wide-field Infrared Survey Explorer (*WISE*) are a reliable and isotropic proxy of the AGN intrinsic luminosity. To do so we have studied the correspondence between the rest-frame  $6\mu\text{m}$  and intrinsic 2-10 keV continuum luminosities of AGN using a complete, X-ray flux limited sample of 137 type 1 AGN and 95 type 2 AGN drawn from the Bright Ultra-hard XMM-Newton Survey. The AGN in this study have 2-10 keV X-ray luminosities between  $10^{42}$  and  $10^{46}$  erg s $^{-1}$ ,  $z$  in the range 0.05-2.8 with a median  $z$  of 0.558 and Compton-thin X-ray absorption. The X-ray luminosities were computed from a detailed analysis of the good quality *XMM-Newton* spectra available for all objects and are corrected for absorption. To compute the mid-IR continuum emission associated with the AGN dusty torus at rest-frame  $6\mu\text{m}$  we decomposed the rest-frame UV-to-mid-IR SEDs of our AGN into AGN and host galaxy components.

To determine the existing relationship between  $L_{6\mu\text{m}}$  and  $L_{2-10\text{keV}}$  luminosities, we have conducted a linear regression analysis in log-log space using the Bayesian max-

imum likelihood technique proposed by Kelly (2007). The main results of our study can be summarized as follows:

(i) We find that at AGN luminosities  $L_{2-10\text{keV}} > 10^{42}$  erg s $^{-1}$ , the mid-IR emission detected with *WISE* at rest-frame  $\sim 6\mu\text{m}$  is dominated by hot dust heated by the AGN. The contamination from the AGN host galaxies and the accretion disk at these wavelengths is not negligible, at a  $\sim 30$  per cent level for AGN with  $10^{42} < L_{2-10\text{keV}} < 10^{43}$  erg s $^{-1}$  and at a  $\sim 12$ -18 per cent level for AGN with  $10^{43} < L_{2-10\text{keV}} < 10^{46}$  erg s $^{-1}$ .

(ii) We also found a relationship for the full AGN sample that is consistent with being linear,  $L_{6\mu\text{m}} \propto L_{2-10\text{keV}}^{0.99 \pm 0.03}$ , but has significant intrinsic scatter,  $\Delta \log L_{6\mu\text{m}} \sim 0.35$  dex. At a given X-ray luminosity, both the intrinsic scatter in  $6\mu\text{m}$  luminosities and the slopes of the linear regression relations are compatible, within the uncertainties, for both type 1 and type 2 AGN.

(iii) The main contributors to the intrinsic scatter in the  $L_{6\mu\text{m}}$  versus  $L_{2-10\text{keV}}$  correlation are likely the well known large dispersion in the individual SED shapes associated with the varying properties of the material responsible for the X-ray and mid-IR emission and AGN variability. If the AGN dust emission at rest-frame wavelengths  $< 12\mu\text{m}$  is not isotropic, as predicted by models of the AGN dusty tori, such effect should also contribute to the measured intrinsic dispersion.

(iv) Assuming both that the 2-10 keV intrinsic luminosity is a reliable proxy for the AGN bolometric radiative power and a constant X-ray bolometric correction, the fraction of AGN bolometric luminosity that is reprocessed in the mid-IR decreases weakly, if at all, with the AGN luminosity over the three decades in X-ray luminosity covered with our sample. This finding is at odds with simple receding torus models.

(v) The  $\log(L_{6\mu\text{m}}/L_{2-10\text{keV}})$  luminosity ratio is largely independent of the line-of-sight X-ray absorption. If the material that absorbs the X-rays re-emits the radiation almost isotropically, we should observe approximately the same  $\log(L_{6\mu\text{m}}/L_{2-10\text{keV}})$  value regardless of orientation, yet the X-ray absorption along the line-of-sight to the AGN could differ significantly. We have shown that the AGN emission at rest-frame  $6\mu\text{m}$  is not free of dust extinction effects. Nevertheless, taking into account the large overlap between the  $\log(L_{6\mu\text{m}}/L_{12\mu\text{m}})$  distributions for the type 1 and type 2 AGN populations ( $\sim 0.1$  dex of shift) and the significant scatter in the luminosity ratio distributions, any orientation-dependent effects, such as a correlation with the line-of-sight X-ray absorption, will certainly be difficult to detect, at least for AGN with X-ray absorption in the Compton-thin regime.

(vi) Type 2 AGN have on average redder mid-IR continua and, at a given X-ray luminosity, are  $\sim 1.3$ -2 times fainter at rest-frame  $6\mu\text{m}$  than type 1 AGN, although with a considerable overlap between both populations. If the AGN X-ray emission is weakly anisotropic, as recent results suggest, a correction for such effect would increase the differences in mid-IR luminosities at a given X-ray luminosity between type 1 and type 2 AGN.

Regardless of whether all AGN have the same or different nuclear dusty toroidal structures, our results imply that the AGN emission at rest-frame  $6\mu\text{m}$  is not completely isotropic due to self-absorption in the dusty torus. Thus our



results imply that AGN surveys at rest-frame  $\sim 6\ \mu\text{m}$  are subject to modest dust obscuration biases.

## ACKNOWLEDGMENTS

This work is based on observations obtained with XMM-Newton, an ESA science mission with instruments and contributions directly funded by ESA Member States and NASA. Based on data from the Wide-field Infrared Survey Explorer, which is a joint project of the University of California, Los Angeles, and the Jet Propulsion Laboratory/California Institute of Technology, funded by the National Aeronautics and Space Administration. Funding for the SDSS and SDSS-II has been provided by the Alfred P. Sloan Foundation, the Participating Institutions, the National Science Foundation, the U.S. Department of Energy, the National Aeronautics and Space Administration, the Japanese Monbukagakusho, the Max Planck Society and the Higher Education Funding Council for England. The SDSS Web Site is <http://www.sdss.org/>. Based on observations collected at the European Organization for Astronomical Research in the Southern hemisphere, Chile, programme IDs 084.A-0828, 086.A-0612, 087.A-0447 and 088.A-0628. Based on observations made with the William Herschel Telescope and its service programme (programme IDs: SW2009a17, SW2009b15, SW2010b20)- operated by the Isaac Newton Group, the Telescopio Nazionale Galileo (programme IDs: TNG12-09B, TNG15-10A, TNG11-10B, TNG12-11A) - operated by the Centro Galileo Galilei and the Gran Telescopio de Canarias (programme IDs: GTC38-09B, GTC32-10A, GTC18-10B, GTC44-11A, GTC41-12A, GTC25-13A) installed in the Spanish Observatorio del Roque de los Muchachos of the Instituto de Astrofísica de Canarias, in the island of La Palma. SM, FJC, XB, A.H.-C. and A.A.-H. acknowledge financial support by the Spanish Ministry of Economy and Competitiveness through grant AYA2012-31447. SM, FJC and A.A.-H. acknowledge financial support from the ARCHES project (7th Framework of the European Union, No. 313146). AA-H acknowledges support from the Universidad de Cantabria through the Augusto G. Linares program. AC, RDC and PS acknowledge financial support from the Italian Ministry of Education, Universities and Research (PRIN2010-2011, grant n. 2010NHBSBE) and from ASI (grant n. I/088/06/0). The authors wish to thank the anonymous referee for constructive comments.

## REFERENCES

- Abazajian K. N., et al., 2009, *ApJS*, 182, 543  
 Alonso-Herrero A., et al., 2011, *ApJ*, 736, 82  
 Alonso-Herrero A., et al., 2006, *ApJ*, 640, 167  
 Alonso-Herrero A., Quillen A. C., Rieke G. H., Ivanov V. D., Efstathiou A., 2003, *AJ*, 126, 81  
 Alonso-Herrero A., Ward M. J., Kotilainen J. K., 1996, *MNRAS*, 278, 902  
 Antonucci R., 1993, *ARA&A*, 31, 473  
 Arnaud K. A., 1996, *ASPC*, 101, 17  
 Asmus D., Hönig S. F., Gandhi P., Smette A., Duschl W. J., 2014, *MNRAS*, 439, 1648  
 Asmus D., Gandhi P., Smette A., Hönig S. F., Duschl W. J., 2011, *A&A*, 536, A36  
 Assef R. J., et al., 2013, *ApJ*, 772, 26  
 Assef R. J., et al., 2010, *ApJ*, 713, 970  
 Ballo L., Severgnini P., Della Ceca R., Caccianiga A., Vignali C., Carrera F. J., Corral A., Mateos S., 2014, *MNRAS*, 444, 2580  
 Barcons X., Franceschini A., de Zotti G., Danese L., Miyaji T., 1995, *ApJ*, 455, 480  
 Bianchi S., Bonilla N. F., Guainazzi M., Matt G., Ponti G., 2009, *A&A*, 501, 915  
 Bruzual G., Charlot S., 2003, *MNRAS*, 344, 1000  
 Caccianiga A., et al., 2008, *A&A*, 477, 735  
 Caccianiga A., Severgnini P., Della Ceca R., Maccacaro T., Carrera F. J., Page M. J., 2007, *A&A*, 470, 557  
 Calderone G., Sbarrato T., Ghisellini G., 2012, *MNRAS*, 425, L41  
 Calzetti D., Armus L., Bohlin R. C., Kinney A. L., Koornneef J., Storchi-Bergmann T., 2000, *ApJ*, 533, 682  
 Cardelli J. A., Clayton G. C., Mathis J. S., 1989, *ApJ*, 345, 245  
 Chabrier G., 2003, *ApJ*, 586, L133  
 Cohen M., Wheaton W. A., Megeath S. T., 2003, *AJ*, 126, 1090  
 Corral A., Della Ceca R., Caccianiga A., Severgnini P., Brunner H., Carrera F. J., Page M. J., Schwöpe A. D., 2011, *A&A*, 530, A42  
 Cutri R. M., et al., 2013, Technical Report, Explanatory Supplement to the AllWISE Data Release Products  
 Cutri R. M., et al., 2003, The IRSA 2MASS All-Sky Point Source Catalog, NASA/IPAC Infrared Science Archive, available at: <http://irsa.ipac.caltech.edu/applications/Gator/>  
 Della Ceca R., et al., 2008, *A&A*, 487, 119  
 Diamond-Stanic A. M., Rieke G. H., Rigby J. R., 2009, *ApJ*, 698, 623  
 Dicken D., et al., 2014, *ApJ*, 788, 98  
 Dickey J. M., Lockman F. J., 1990, *ARA&A*, 28, 215  
 Elbaz D., et al., 2011, *A&A*, 533, A119  
 Elvis M., et al., 1994, *ApJS*, 95, 1  
 Fanali R., Caccianiga A., Severgnini P., Della Ceca R., Marchese E., Carrera F. J., Corral A., Mateos S., 2013, *MNRAS*, 433, 648  
 Feltre A., Hatziminaoglou E., Fritz J., Franceschini A., 2012, *MNRAS*, 426, 120  
 Fiore F., et al., 2009, *ApJ*, 693, 447  
 Fritz J., Franceschini A., Hatziminaoglou E., 2006, *MNRAS*, 366, 767  
 Gandhi P., Horst H., Smette A., Hönig S., Comastri A., Gilli R., Vignali C., Duschl W., 2009, *A&A*, 502, 457  
 Gordon K. D., Clayton G. C., 1998, *ApJ*, 500, 816  
 Granato G. L., Danese L., 1994, *MNRAS*, 268, 235  
 Guainazzi M., Matt G., Perola G. C., 2005, *A&A*, 444, 119  
 Hernán-Caballero A., et al., 2009, *MNRAS*, 395, 1695  
 Hewett P. C., Warren S. J., Leggett S. K., Hodgkin S. T., 2006, *MNRAS*, 367, 454  
 Hönig S. F., Leipski C., Antonucci R., Haas M., 2011, *ApJ*, 736, 26  
 Hopkins P. F., Richards G. T., Hernquist L., 2007, *ApJ*, 654, 731  
 Hopkins P. F., et al., 2004, *AJ*, 128, 1112  
 Horst H., Gandhi P., Smette A., Duschl W. J., 2008, *A&A*,

- 479, 389
- Ichikawa K., Ueda Y., Terashima Y., Oyabu S., Gandhi P., Matsuta K., Nakagawa T., 2012, *ApJ*, 754, 45
- Isoe T., Feigelson E. D., Akritas M. G., Babu G. J., 1990, *ApJ*, 364, 104
- Jarrett T. H., Chester T., Cutri R., Schneider S., Skrutskie M., Huchra J. P., 2000, *AJ*, 119, 2498
- Kelly B. C., 2007, *ApJ*, 665, 1489
- Kennicutt R. C., Jr., 1998, *ARA&A*, 36, 189
- Kotilainen J. K., Ward M. J., Boisson C., Depoy D. L., Smith M. G., Bryant L. R., 1992, *MNRAS*, 256, 125
- Krabbe A., Böker T., Maiolino R., 2001, *ApJ*, 557, 626
- Lacy M., et al., 2013, *ApJS*, 208, 24
- LaMassa S. M., Heckman T. M., Ptak A., Martins L., Wild V., Sonnentrucker P., 2010, *ApJ*, 720, 786
- Lawrence A., et al., 2007, *MNRAS*, 379, 1599
- Lawrence A., 1991, *MNRAS*, 252, 586
- Levenson N. A., Radomski J. T., Packham C., Mason R. E., Schaefer J. J., Telesco C. M., 2009, *ApJ*, 703, 390
- Liu T., Wang J.-X., Yang H., Zhu F.-F., Zhou Y.-Y., 2014, *ApJ*, 783, 106
- Lusso E., et al., 2013, *ApJ*, 777, 86
- Lutz D., Maiolino R., Spoon H. W. W., Moorwood A. F. M., 2004, *A&A*, 418, 465
- Mainieri V., Bergeron J., Hasinger G., Lehmann I., Rosati P., Schmidt M., Szokoly G., Della Ceca R., 2002, *A&A*, 393, 425
- Maiolino R., Shemmer O., Imanishi M., Netzer H., Oliva E., Lutz D., Sturm E., 2007, *A&A*, 468, 979
- Maiolino R., Marconi A., Salvati M., Risaliti G., Severgnini P., Oliva E., La Franca F., Vanzi L., 2001, *A&A*, 365, 28
- Marchese E., Della Ceca R., Caccianiga A., Severgnini P., Corral A., Fanali R., 2012, *A&A*, 539, A48
- Marconi A., Risaliti G., Gilli R., Hunt L. K., Maiolino R., Salvati M., 2004, *MNRAS*, 351, 169
- Martínez-Sansigre A., Rawlings S., Lacy M., Fadda D., Marleau F. R., Simpson C., Willott C. J., Jarvis M. J., 2005, *Natur*, 436, 666
- Mason R. E., et al., 2012, *AJ*, 144, 11
- Mateos S., Alonso-Herrero A., Carrera F. J., Blain A., Severgnini P., Caccianiga A., Ruiz A., 2013, *MNRAS*, 434, 941
- Mateos S., et al., 2012, *MNRAS*, 426, 3271
- Mateos S., et al., 2010, *A&A*, 510, A35
- Mateos S., et al., 2008, *A&A*, 492, 51
- Mateos S., Barcons X., Carrera F. J., Ceballos M. T., Hasinger G., Lehmann I., Fabian A. C., Streblyanska A., 2005b, *A&A*, 444, 79
- Mateos S., et al., 2005a, *A&A*, 433, 855
- Matsuta K., et al., 2012, *ApJ*, 753, 104
- McKernan B., Ford K. E. S., Chang N., Reynolds C. S., 2009, *MNRAS*, 394, 491
- Merloni A., et al., 2014, *MNRAS*, 437, 3550
- Merloni A., K rding E., Heinz S., Markoff S., Di Matteo T., Falcke H., 2006, *NewA*, 11, 567
- Mor R., Netzer H., Elitzur M., 2009, *ApJ*, 705, 298
- Neenkova M., Sirocky M. M., Nikutta R., Ivezić Ž., Elitzur M., 2008b, *ApJ*, 685, 160
- Neenkova M., Sirocky M. M., Ivezić Ž., Elitzur M., 2008a, *ApJ*, 685, 147
- Neugebauer G., Oke J. B., Becklin E. E., Matthews K., 1979, *ApJ*, 230, 79
- Peeters E., Spoon H. W. W., Tielens A. G. G. M., 2004, *ApJ*, 613, 986
- Piconcelli E., Jimenez-Bail n E., Guainazzi M., Schartel N., Rodr guez-Pascual P. M., Santos-Lle  M., 2005, *A&A*, 432, 15
- Pier E. A., Krolik J. H., 1992, *ApJ*, 401, 99
- Pineau F.-X., Motch C., Carrera F., Della Ceca R., Derri re S., Michel L., Schwobe A., Watson M. G., 2011, *A&A*, 527, A126
- Porquet D., Reeves J. N., O'Brien P., Brinkmann W., 2004, *A&A*, 422, 85
- Press W. H., Teukolsky S. A., Vetterling W. T., Flannery B. P., 1992, *nrfa.book*,
- Ramos Almeida C., et al., 2011, *ApJ*, 731, 92
- Ramos Almeida C., P rez Garc a A. M., Acosta-Pulido J. A., Rodr guez Espinosa J. M., 2007, *AJ*, 134, 2006
- Richards G. T., et al., 2006, *AJ*, 131, 2766
- Roseboom I. G., Lawrence A., Elvis M., Petty S., Shen Y., Hao H., 2013, *MNRAS*, 429, 1494
- Rovilos E., et al., 2014, *MNRAS*, 438, 494
- Scott A. E., Stewart G. C., Mateos S., Alexander D. M., Hutton S., Ward M. J., 2011, *MNRAS*, 417, 992
- Scott A. E., Stewart G. C., Mateos S., 2012, *MNRAS*, 423, 2633
- Silva L., Maiolino R., Granato G. L., 2004, *MNRAS*, 355, 973
- Simpson C., 2005, *MNRAS*, 360, 565
- Stern D., et al., 2012, *ApJ*, 753, 30
- Tozzi P., et al., 2006, *A&A*, 451, 457
- Treister E., Krolik J. H., Dullemond C., 2008, *ApJ*, 679, 140
- Turner T. J., George I. M., Nandra K., Mushotzky R. F., 1997, *ApJS*, 113, 23
- Urry C. M., Padovani P., 1995, *PASP*, 107, 803
- Vasudevan R. V., Fabian A. C., 2007, *MNRAS*, 381, 1235
- Winter L. M., Veilleux S., McKernan B., Kallman T. R., 2012, *ApJ*, 745, 107
- Winter L. M., Mushotzky R. F., Reynolds C. S., Tueller J., 2009, *ApJ*, 690, 1322
- Wright E. L., Eisenhardt P. R. M., Mainzer A. K., et al. 2010, *AJ*, 140, 1868
- Yan L., et al., 2013, *AJ*, 145, 55
- Yang H., Wang J., Liu T., 2014, *arXiv*, arXiv:1411.4585

## APPENDIX A: TABLE OF THE SAMPLE PROPERTIES

Table A1: Properties of the AGN used in this study.

| Name                 | Type | $\log L_{2-10 \text{ keV}}$<br>$\text{erg s}^{-1}$ | $\log L_{6\mu\text{m}}$<br>$\text{erg s}^{-1}$ |
|----------------------|------|--|--|
| 2XMMiJ000441.2+00071 | 1.9  | 42.76±0.05   | 42.49±0.10                                     |
| 2XMMiJ001130.3+00575 | 1    | 45.22±0.02   | 46.15±0.07                                     |
| 2XMMJ002146.3-084711 | 1    | 45.00±0.04   | 45.49±0.10                                     |
| 2XMMiJ002244.5+00182 | 1    | 43.67±0.02   | 43.58±0.16                                     |
| 2XMMJ003430.8-213351 | 1    | 44.21±0.04   | 44.20±0.26                                     |
| 2XMMJ004003.8+005853 | 1    | 44.66±0.15   | 45.55±0.05                                     |
| 2XMMJ004341.4+005610 | 1    | 44.55±0.02   | 44.43±0.27                                     |
| 2XMMJ004404.6+010153 | 2    | 43.48±0.05   | 43.45±0.04                                     |
| 2XMMiJ011829.6+00454 | 1    | 43.74±0.01   | 43.67±0.08                                     |
| 2XMMJ012447.7+320727 | 1    | 45.06±0.03   | 45.43±0.05                                     |
| 2XMMJ013943.0+061254 | 1.5  | 44.46±0.08   | 44.43±0.10                                     |
| 2XMMJ014804.3+055055 | 1    | 42.33±0.06   | 43.21±0.05                                     |
| 2XMMJ020011.5-093125 | 1    | 44.17±0.03   | 44.41±0.04                                     |
| 2XMMJ020112.5-092016 | 2    | 43.33±0.34   | 43.65±0.08                                     |
| 2XMMJ022430.4+185315 | 2    | 43.94±0.14   | 44.33±0.13                                     |
| 2XMMJ023234.3-073102 | 1    | 44.29±0.01   | 45.20±0.05                                     |
| 2XMMJ024200.8+000021 | 1    | 44.84±0.02   | 45.57±0.06                                     |
| 2XMMJ024325.4-000412 | 1.5  | 43.48±0.04   | 43.70±0.17                                     |
| 2XMMJ030419.5-010911 | 2    | 42.93±0.12   | 43.07±0.13                                     |
| 2XMMJ030742.6-000121 | 1.5  | 43.66±0.05   | 43.43±0.16                                     |
| 2XMMJ033729.5+004227 | 1    | 43.61±0.01   | 43.21±0.38                                     |
| 2XMMiJ044710.5-06255 | 1    | 45.49±0.05   | 45.96±0.16                                     |
| 2XMMJ073534.9+435414 | 1.9  | 43.07±0.35   | 43.62±0.09                                     |
| 2XMMiJ075734.4+39260 | 2    | 43.38±0.24   | 43.72±0.02                                     |
| 2XMMJ080411.1+650906 | 2    | 44.35±0.18   | 43.98±0.14                                     |
| 2XMMJ080608.0+244421 | 1    | 43.87±0.01   | 44.55±0.04                                     |
| 2XMMJ081014.5+280337 | 1    | 44.83±0.03   | 45.09±0.07                                     |
| 2XMMJ082042.4+205715 | 2    | 42.60±0.02   | 43.67±0.03                                     |
| 2XMMJ082053.8+210735 | 2    | 44.48±0.24   | 44.62±0.29                                     |
| 2XMMJ083049.6+524910 | 1    | 44.67±0.02   | 44.65±0.30                                     |
| 2XMMJ083139.1+524205 | 2    | 42.34±0.10   | 42.79±0.03                                     |
| 2XMMiJ084012.7+51124 | 1    | 45.99±0.06   | 46.64±0.11                                     |
| 2XMMJ084117.5+003448 | 2    | 42.74±0.31   | 42.95±0.05                                     |
| 2XMMJ084927.7+445458 | 1    | 44.49±0.18   | 45.27±0.06                                     |
| 2XMMJ085228.6+163008 | 2    | 43.54±0.12   | 44.15±0.03                                     |
| 2XMMJ085835.2+275543 | 1    | 43.82±0.29   | 44.20±0.04                                     |
| 2XMMJ085841.4+140944 | 1    | 45.64±0.02   | 45.81±0.06                                     |
| 2XMMJ090053.8+385616 | 2    | 44.04±0.35   | 43.77±0.03                                     |
| 2XMMiJ091557.3+29261 | 1    | 44.00±0.01   | 45.00±0.04                                     |
| 2XMMiJ091624.3+29391 | 1    | 44.92±0.07   | 45.10±0.15                                     |
| 2XMMJ091636.5+301749 | 2    | 42.83±0.02   | 43.46±0.03                                     |
| 2XMMJ091645.4+514146 | 2    | 42.98±0.02   | 43.25±0.06                                     |
| 2XMMJ092129.2+370103 | 1    | 43.16±0.01   | 43.63±0.05                                     |
| 2XMMJ092201.2+301411 | 2    | 44.35±0.23   | 44.00±0.15                                     |
| 2XMMJ092313.0+511742 | 1    | 43.82±0.03   | 43.78±0.11                                     |
| 2XMMiJ092619.6+36271 | 1    | 44.41±0.02   | 45.11±0.06                                     |
| 2XMMJ093347.9+551846 | 1    | 44.75±0.03   | 45.09±0.08                                     |
| 2XMMJ093458.2+611234 | 1.9  | 43.44±0.21   | 43.90±0.16                                     |
| 2XMMJ094057.1+032401 | 1.5  | 42.51±0.02   | 43.08±0.04                                     |
| 2XMMJ094350.2+035913 | 1    | 44.44±0.15   | 45.36±0.05                                     |
| 2XMMJ094404.3+480647 | 1    | 43.62±0.03   | 44.63±0.04                                     |
| 2XMMJ094439.8+034940 | 1    | 43.23±0.03   | 44.21±0.03                                     |
| 2XMMJ094509.0+040817 | 2    | 42.83±0.18   | 43.11±0.05                                     |
| 2XMMiJ095630.7-00343 | 1    | 43.64±0.09   | 43.53±0.07                                     |
| 2XMMJ095732.0+024302 | 1    | 44.57±0.02   | 44.59±0.15                                     |
| 2XMMJ095815.5+014922 | 1    | 45.10±0.01   | 45.39±0.16                                     |
| 2XMMJ095857.3+021314 | 1    | 44.95±0.01   | 44.78±0.17                                     |

Table A1: continued.

| Name                 | Type | $\log L_{2-10 \text{ keV}}$<br>erg s <sup>-1</sup> | $\log L_{6\mu\text{m}}$<br>erg s <sup>-1</sup> |
|----------------------|------|--|--|
| (1)                  | (2)  | (3)  | (4)  |
| 2XMMJ095908.3+024309 | 1    | 45.09±0.02   | 45.38±0.10                                     |
| 2XMMJ095918.7+020951 | 1    | 44.90±0.01   | 45.27±0.09                                     |
| 2XMMJ100015.3+013147 | 2    | 44.68±0.06   | 44.77±0.15                                     |
| 2XMMJ100025.2+015852 | 1.5  | 44.01±0.01   | 44.15±0.05                                     |
| 2XMMJ100032.1+553630 | 2    | 43.58±0.17   | 43.64±0.04                                     |
| 2XMMJ100035.4+052428 | 1.5  | 42.63±0.03   | 43.04±0.03                                     |
| 2XMMJ100057.4+684230 | 1    | 44.00±0.04   | 44.68±0.05                                     |
| 2XMMJ100120.7+555351 | 1    | 46.00±0.01   | 45.97±0.08                                     |
| 2XMMJ100129.3+013633 | 2    | 42.74±0.16   | 43.15±0.03                                     |
| 2XMMJ100205.0+023731 | 1    | 44.19±0.01   | 44.20±0.09                                     |
| 2XMMJ100237.8+024701 | 1.5  | 43.02±0.31   | 44.08±0.03                                     |
| 2XMMJ101616.7+391143 | 1    | 43.74±0.05   | 44.40±0.05                                     |
| 2XMMiJ101733.1-00014 | 1.9  | 43.18±0.02   | 42.77±0.03                                     |
| 2XMMiJ101811.5+00101 | 1    | 44.71±0.05   | 44.87±0.26                                     |
| 2XMMiJ101830.7+00050 | 2    | 42.73±0.06   | 42.53±0.04                                     |
| 2XMMJ101922.6+412050 | 1    | 43.51±0.04   | 43.47±0.07                                     |
| 2XMMJ102147.4+130850 | 1    | 44.34±0.02   | 44.67±0.07                                     |
| 2XMMJ102147.8+131227 | 1.8  | 43.33±0.01   | 43.20±0.03                                     |
| 2XMMJ102551.1+384008 | 1.5  | 42.75±0.01   | 42.71±0.17                                     |
| 2XMMJ103739.4+414149 | 1    | 44.90±0.02   | 44.63±0.20                                     |
| 2XMMJ104048.4+061819 | 1    | 42.79±0.03   | 42.63±0.26                                     |
| 2XMMJ104451.4-012226 | 2    | 44.94±0.06   | 44.90±0.22                                     |
| 2XMMJ104522.0-012844 | 1    | 44.57±0.03   | 45.04±0.06                                     |
| 2XMMJ104522.1+212614 | 1    | 44.55±0.01   | 45.39±0.06                                     |
| 2XMMJ104912.6+330501 | 1.9  | 43.42±0.21   | 43.67±0.05                                     |
| 2XMMJ105250.0+335505 | 1    | 45.20±0.00   | 46.02±0.07                                     |
| 2XMMJ105932.0+242939 | 1    | 44.71±0.02   | 45.10±0.08                                     |
| 2XMMiJ111006.8+61252 | 1    | 43.56±0.03   | 44.59±0.03                                     |
| 2XMMJ111121.2+482333 | 1    | 44.70±0.05   | 44.99±0.07                                     |
| 2XMMJ111121.6+482047 | 1    | 43.65±0.06   | 44.58±0.03                                     |
| 2XMMJ111135.6+482945 | 1    | 44.67±0.01   | 44.82±0.05                                     |
| 2XMMJ111559.0+425321 | 1    | 44.83±0.03   | 45.26±0.11                                     |
| 2XMMJ111606.9+423645 | 1    | 44.55±0.01   | 44.64±0.08                                     |
| 2XMMJ111750.7+075710 | 1.5  | 44.74±0.01   | 44.70±0.08                                     |
| 2XMMJ111832.4+130732 | 1    | 44.39±0.08   | 44.59±0.15                                     |
| 2XMMJ111909.2+130950 | 2    | 44.54±0.27   | 44.80±0.08                                     |
| 2XMMJ112026.6+431519 | 2    | 43.12±0.28   | 43.23±0.04                                     |
| 2XMMJ112328.0+052823 | 1    | 42.71±0.02   | 43.69±0.03                                     |
| 2XMMJ112338.0+052038 | 1    | 45.60±0.06   | 45.72±0.20                                     |
| 2XMMJ113121.7+310254 | 1.9  | 43.41±0.05   | 43.40±0.05                                     |
| 2XMMJ113129.2+310944 | 1    | 43.26±0.01   | 43.15±0.30                                     |
| 2XMMiJ114654.6+20254 | 1    | 44.78±0.03   | 44.92±0.21                                     |
| 2XMMJ115754.9+434753 | 2    | 42.58±0.06   | 42.97±0.03                                     |
| 2XMMJ120518.6+443926 | 1.9  | 43.60±0.02   | 43.66±0.07                                     |
| 2XMMJ120529.5+442106 | 1    | 43.66±0.12   | 44.55±0.04                                     |
| 2XMMJ120952.6+393143 | 1    | 42.89±0.08   | 43.66±0.03                                     |
| 2XMMJ121118.8+503653 | 1.9  | 43.38±0.04   | 43.76±0.02                                     |
| 2XMMJ121122.4+130936 | 1    | 43.86±0.02   | 44.49±0.03                                     |
| 2XMMJ121356.1+140431 | 1    | 43.44±0.06   | 43.61±0.04                                     |
| 2XMMJ121422.9+024252 | 1    | 45.85±0.02   | 46.38±0.10                                     |
| 2XMMJ121509.4+135450 | 1    | 44.50±0.02   | 45.36±0.06                                     |
| 2XMMJ121732.7+465829 | 1    | 45.32±0.03   | 46.12±0.10                                     |
| 2XMMJ121808.5+471613 | 1    | 43.85±0.01   | 43.93±0.07                                     |
| 2XMMJ121839.4+470627 | 2    | 43.09±0.25   | 43.78±0.03                                     |
| 2XMMJ121920.6+470323 | 2    | 43.46±0.20   | 44.14±0.06                                     |
| 2XMMJ121930.9+064334 | 1    | 42.98±0.02   | 43.65±0.08                                     |
| 2XMMJ121952.2+472058 | 1    | 44.41±0.01   | 44.74±0.06                                     |



Table A1: continued.

| Name                 | Type | $\log L_{2-10 \text{ keV}}$<br>erg s <sup>-1</sup> | $\log L_{6\mu\text{m}}$<br>erg s <sup>-1</sup> |
|----------------------|------|--|--|
| (1)                  | (2)  | (3)  | (4)  |
| 2XMMJ122132.3+043557 | 1    | 45.13±0.06   | 44.77±0.59                                     |
| 2XMMJ122137.8+043025 | 1.5  | 42.85±0.02   | 43.53±0.05                                     |
| 2XMMJ122330.7+154507 | 1    | 42.69±0.02   | 43.07±0.04                                     |
| 2XMMJ122532.4+332532 | 1    | 44.11±0.01   | 44.07±0.14                                     |
| 2XMMJ122649.5+311735 | 1.9  | 42.82±0.04   | 42.71±0.04                                     |
| 2XMMJ122656.4+013124 | 1.8  | 44.61±0.12   | 45.12±0.06                                     |
| 2XMMJ123149.0+214749 | 2    | 43.23±0.02   | 43.29±0.08                                     |
| 2XMMJ123204.9+215254 | 2    | 45.19±0.10   | 45.15±0.06                                     |
| 2XMMJ123305.8+001438 | 1    | 43.40±0.01   | 42.89±0.29                                     |
| 2XMMJ123356.1+074755 | 1.5  | 44.12±0.01   | 43.97±0.08                                     |
| 2XMMJ123412.7+372734 | 2    | 43.72±0.09   | 44.31±0.03                                     |
| 2XMMiJ123602.1+26182 | 2    | 43.53±0.07   | 43.74±0.05                                     |
| 2XMMiJ123604.0+26413 | 1    | 43.59±0.01   | 44.55±0.03                                     |
| 2XMMJ123625.4+125844 | 2    | 42.78±0.06   | 42.91±0.04                                     |
| 2XMMJ123725.2+114158 | 1    | 44.08±0.02   | 43.87±0.32                                     |
| 2XMMJ123759.5+621102 | 1    | 44.59±0.01   | 45.08±0.07                                     |
| 2XMMJ124127.1+331201 | 2    | 43.96±0.06   | 43.67±0.36                                     |
| 2XMMJ124135.8+332624 | 2    | 42.98±0.38   | 43.75±0.03                                     |
| 2XMMJ124205.1+323634 | 2    | 44.43±0.25   | 44.49±0.10                                     |
| 2XMMJ124213.8-112510 | 1    | 44.42±0.02   | 44.83±0.09                                     |
| 2XMMJ124301.0+131217 | 2    | 43.05±0.02   | 43.08±0.18                                     |
| 2XMMJ124408.9+113334 | 1.5  | 43.69±0.01   | 43.86±0.07                                     |
| 2XMMJ124540.9-002744 | 1    | 45.30±0.03   | 45.76±0.11                                     |
| 2XMMJ125304.6+101239 | 2    | 44.67±0.73   | 44.44±0.04                                     |
| 2XMMJ125357.1+154314 | 2    | 44.41±0.11   | 44.56±0.18                                     |
| 2XMMJ125414.5+101605 | 2    | 42.80±0.08   | 43.40±0.03                                     |
| 2XMMJ125453.1+272008 | 2    | 43.37±0.17   | 44.54±0.03                                     |
| 2XMMJ125553.0+272405 | 1    | 44.02±0.01   | 44.24±0.04                                     |
| 2XMMJ125610.4+260103 | 1    | 44.85±0.02   | 45.19±0.10                                     |
| 2XMMJ130237.6-024055 | 2    | 43.12±0.06   | 43.65±0.03                                     |
| 2XMMJ130619.0+672421 | 2    | 43.34±0.12   | 43.47±0.03                                     |
| 2XMMiJ130906.2+11330 | 2    | 44.59±0.24   | 45.18±0.07                                     |
| 2XMMJ130936.2+082815 | 1    | 44.52±0.13   | 44.67±0.09                                     |
| 2XMMJ131046.7+271645 | 1    | 44.20±0.01   | 44.00±0.05                                     |
| 2XMMiJ131213.6+23195 | 1    | 45.12±0.11   | 46.02±0.08                                     |
| 2XMMJ132037.8+341126 | 1    | 42.33±0.03   | 42.80±0.08                                     |
| 2XMMJ132101.4+340658 | 1    | 43.78±0.04   | 44.17±0.04                                     |
| 2XMMJ132105.4+341500 | 1    | 44.01±0.04   | 43.97±0.09                                     |
| 2XMMJ132349.6+654148 | 1    | 43.99±0.01   | 44.63±0.03                                     |
| 2XMMJ132419.0+300042 | 2    | 42.12±0.04   | 42.46±0.03                                     |
| 2XMMJ132447.4+300900 | 2    | 44.28±0.11   | 44.43±0.08                                     |
| 2XMMJ132826.3+583420 | 2    | 43.20±0.17   | 43.24±0.08                                     |
| 2XMMJ132958.6+242435 | 1    | 44.36±0.02   | 44.40±0.10                                     |
| 2XMMJ133120.3+242304 | 2    | 44.29±0.02   | 44.17±0.20                                     |
| 2XMMJ133614.8+520224 | 2    | 44.42±0.08   | 45.25±0.06                                     |
| 2XMMJ133811.2+515736 | 2    | 42.92±0.08   | 43.19±0.04                                     |
| 2XMMJ134044.5-004516 | 1    | 43.87±0.02   | 44.79±0.04                                     |
| 2XMMJ134113.9-005314 | 1    | 44.38±0.01   | 44.59±0.03                                     |
| 2XMMJ134133.0-004033 | 2    | 44.31±0.08   | 44.77±0.05                                     |
| 2XMMJ134133.1+353252 | 1    | 44.60±0.02   | 44.76±0.08                                     |
| 2XMMJ134245.8+403913 | 2    | 42.95±0.15   | 43.34±0.03                                     |
| 2XMMJ134252.9+403202 | 1    | 44.69±0.01   | 44.87±0.08                                     |
| 2XMMJ134256.5+000057 | 1    | 44.68±0.02   | 44.35±0.16                                     |
| 2XMMJ134323.6+001223 | 1    | 44.61±0.04   | 44.87±0.09                                     |
| 2XMMJ134511.9+554759 | 1    | 44.82±0.04   | 45.24±0.08                                     |
| 2XMMJ134656.6+580316 | 2    | 43.82±0.07   | 44.62±0.04                                     |
| 2XMMJ134749.8+582109 | 1    | 45.04±0.01   | 45.45±0.05                                     |

Table A1: continued.

| Name                 | Type | $\log L_{2-10 \text{ keV}}$<br>erg s <sup>-1</sup> | $\log L_{6\mu\text{m}}$<br>erg s <sup>-1</sup> |
|----------------------|------|--|--|
| (1)                  | (2)  | (3)  | (4)  |
| 2XMMJ134803.8-035619 | 2    | 44.51±0.42   | 44.58±0.09                                     |
| 2XMMiJ135436.3+05152 | 2    | 42.46±0.24   | 42.72±0.03                                     |
| 2XMMiJ135453.5+05071 | 2    | 43.95±0.91   | 43.73±0.17                                     |
| 2XMMJ135527.6+181639 | 2    | 44.34±0.06   | 44.31±0.06                                     |
| 2XMMJ135628.7+052144 | 2    | 43.49±0.23   | 43.95±0.04                                     |
| 2XMMJ140127.6+025606 | 1    | 43.88±0.01   | 43.91±0.09                                     |
| 2XMMJ140145.0+025332 | 2    | 43.45±0.03   | 43.98±0.04                                     |
| 2XMMJ140248.0+541350 | 2    | 44.49±0.05   | 44.04±0.08                                     |
| 2XMMJ140353.8+540939 | 1.9  | 43.52±0.14   | 43.46±0.09                                     |
| 2XMMJ140515.4+542459 | 1.9  | 42.51±0.14   | 42.34±0.07                                     |
| 2XMMJ140614.2+282340 | 2    | 43.10±0.19   | 42.69±0.07                                     |
| 2XMMJ140716.7+281653 | 2    | 43.21±0.05   | 43.43±0.18                                     |
| 2XMMJ140719.3+281814 | 1    | 45.09±0.02   | 45.55±0.06                                     |
| 2XMMJ140745.3+283028 | 1    | 44.70±0.07   | 44.89±0.05                                     |
| 2XMMJ140921.1+261337 | 1    | 44.89±0.04   | 44.88±0.12                                     |
| 2XMMJ141449.5+361239 | 1.5  | 42.74±0.02   | 43.13±0.08                                     |
| 2XMMJ141512.6+360813 | 1.9  | 43.13±0.02   | 43.70±0.06                                     |
| 2XMMJ141531.4+113156 | 1    | 43.59±0.01   | 44.01±0.03                                     |
| 2XMMJ141622.4+265631 | 2    | 43.22±0.18   | 43.22±0.04                                     |
| 2XMMJ141731.0+265622 | 2    | 43.84±0.60   | 43.80±0.03                                     |
| 2XMMiJ142656.4+60290 | 1    | 44.18±0.02   | 45.20±0.05                                     |
| 2XMMJ142759.5+262150 | 1    | 44.69±0.02   | 44.98±0.07                                     |
| 2XMMJ143025.8+415957 | 1    | 43.72±0.06   | 44.26±0.04                                     |
| 2XMMJ143623.8+631726 | 2    | 44.86±0.06   | 44.90±0.07                                     |
| 2XMMJ144336.1+062802 | 1    | 44.89±0.06   | 45.21±0.19                                     |
| 2XMMJ144404.5+291412 | 1    | 44.41±0.02   | 45.24±0.05                                     |
| 2XMMJ144411.3+291508 | 1    | 44.18±0.18   | 44.14±0.08                                     |
| 2XMMJ144545.5+292312 | 2    | 43.66±0.21   | 44.41±0.04                                     |
| 2XMMJ144936.5+090829 | 1    | 45.03±0.01   | 45.17±0.10                                     |
| 2XMMJ145426.6+182956 | 1    | 43.21±0.03   | 44.32±0.03                                     |
| 2XMMJ145442.2+182937 | 2    | 42.86±0.14   | 43.41±0.03                                     |
| 2XMMJ145459.4+184452 | 1    | 44.46±0.03   | 44.68±0.05                                     |
| 2XMMJ145717.5+223332 | 1    | 44.60±0.03   | 44.47±0.15                                     |
| 2XMMJ150431.2+474151 | 1    | 45.00±0.01   | 44.68±0.08                                     |
| 2XMMJ150558.3+014104 | 2    | 43.20±0.24   | 43.50±0.05                                     |
| 2XMMiJ150743.3+01132 | 1    | 45.25±0.06   | 45.91±0.07                                     |
| 2XMMJ150930.9+565454 | 1    | 45.15±0.09   | 46.05±0.07                                     |
| 2XMMJ151536.7+000347 | 2    | 43.16±0.09   | 43.85±0.04                                     |
| 2XMMJ151703.6+562338 | 1.5  | 43.93±0.01   | 43.62±0.19                                     |
| 2XMMJ152721.7+360016 | 2    | 43.49±0.27   | 43.54±0.05                                     |
| 2XMMJ153202.2+301629 | 2    | 42.84±0.01   | 42.47±0.06                                     |
| 2XMMJ153228.8+045358 | 1.5  | 44.08±0.01   | 44.30±0.03                                     |
| 2XMMJ153304.0+302508 | 1.8  | 43.19±0.18   | 43.52±0.05                                     |
| 2XMMJ154424.1+535546 | 2    | 44.00±0.25   | 44.48±0.04                                     |
| 2XMMJ154930.6+213422 | 2    | 44.12±0.10   | 43.82±0.21                                     |
| 2XMMiJ155850.7+02353 | 1    | 44.62±0.03   | 44.36±0.19                                     |
| 2XMMJ163331.8+570520 | 1    | 43.64±0.01   | 44.01±0.06                                     |
| 2XMMJ164119.4+385407 | 1    | 43.39±0.02   | 43.74±0.08                                     |
| 2XMMJ164203.4+385300 | 1    | 43.82±0.03   | 43.74±0.17                                     |
| 2XMMiJ164723.9+27054 | 2    | 43.87±0.11   | 43.94±0.04                                     |
| 2XMMiJ173104.7+36580 | 1.9  | 43.37±0.12   | 43.47±0.05                                     |
| 2XMMJ200812.3-111658 | 2    | 44.48±0.10   | 43.96±0.22                                     |
| 2XMMJ204043.2-004548 | 2    | 44.42±0.13   | 44.62±0.08                                     |
| 2XMMJ204956.3-053457 | 2    | 43.55±0.18   | 43.98±0.05                                     |
| 2XMMJ205038.3-053134 | 2    | 42.85±0.18   | 42.80±0.09                                     |
| 2XMMJ211516.5+060840 | 1    | 43.93±0.02   | 44.67±0.04                                     |
| 2XMMJ212932.8+001044 | 1.9  | 43.08±0.03   | 43.16±0.04                                     |

Table A1: continued.

| Name                 | Type | $\log L_{2-10 \text{ keV}}$<br>erg s <sup>-1</sup> | $\log L_{6\mu\text{m}}$<br>erg s <sup>-1</sup> |
|----------------------|------|--|--|
| (1)                  | (2)  | (3)  | (4)  |
| 2XMMiJ215017.3-05571 | 2    | 42.66±0.11   | 42.73±0.04                                     |
| 2XMMiJ215138.7-05224 | 1    | 44.47±0.02   | 44.86±0.19                                     |
| 2XMMJ221813.9+001624 | 2    | 43.72±0.37   | 43.86±0.06                                     |
| 2XMMiJ232807.6+14420 | 1    | 43.47±0.09   | 43.85±0.03                                     |

*Notes.* The targets are listed in order of increasing right ascension. Column 1: X-ray source name as listed in the second incremental version of the Second XMM-Newton Serendipitous Source Catalogue (2XMM-DR3; [http://xmmssc-www.star.le.ac.uk/Catalogue/xcat\\_public\\_2XMMi-DR3.html](http://xmmssc-www.star.le.ac.uk/Catalogue/xcat_public_2XMMi-DR3.html)); Column 2: optical spectroscopic classification. <sup>a</sup>for objects with a galaxy UV/optical spectrum without emission lines; Column 3: 2-10 keV X-ray luminosity and  $1\sigma$  uncertainty (in logarithmic units). The luminosities have been corrected for X-ray absorption. Column 4: rest-frame  $6\mu\text{m}$  AGN luminosity associated to the dusty torus emission and  $1\sigma$  uncertainty (in logarithmic units). The infrared luminosities have been corrected for both the accretion disk and host galaxy emission.

This paper has been typeset from a  $\text{\TeX}$ / $\text{\LaTeX}$  file prepared by the author.